COLLEGE OF ENGINEERING
NUCLEAR ENGINEERING & RADIOLOGICAL SCIENCES
UNIVERSITY OF MICHIGAN

Nuclear Reactor
Analysis & Methods
Group
NuRAM

NE/8887/2020-004-00
NURAM-2020-006-00

Point Kinetics Model Development with Predictive Control for Multi-Module HTGR Special Purpose Reactors

Sooyoung Choi, Shai Kinast, and Brendan Kochunas

University of Michigan

12/29/2020

NEUP Nuclear Energy University Program
U.S. Department of Energy

This page is intentionally blank.

REVISION LOG

Revision	Date	Affected Pages	Revision Description
0	12/29/2020	All	Initial Release

Document pages that are:

Export Controlled:	No
IP/Proprietary/NDA Controlled:	No
Sensitive Controlled:	No
Unlimited:	Yes

This work was supported by funding received from the DOE Office of Nuclear Energy's Nuclear Energy University Program under contract number DE-NE0008887.

COLLEGE OF ENGINEERING
NUCLEAR ENGINEERING & RADIOLOGICAL SCIENCES
UNIVERSITY OF MICHIGAN

Argonne NATIONAL LABORATORY

HolosGen™

EXECUTIVE SUMMARY

In this report we document the development of a state-space dynamics model and control algorithms that may actively provide autonomous reactivity control of a microreactor. This builds on our previous work that performed the simulations necessary to obtain coefficients to evaluate the state-space model.

The purpose of developing the state-space model and control algorithms is to provide a reference for how well existing control technologies will function given the task of reactivity control of a microreactor. The basis of the model presented within are the point kinetics equations coupled with a three-temperature thermal-hydraulics model. We derive the state-space representation of this model, and associated transfer function. The model is first used to study the reactor stability analytically through the formalisms of the Bode diagram and root locus method. These results show that:

- the Holos reactor is linearly stable
- the dynamic response is similar to the zero power reactor transfer function
- when compared with the zero power reactor, the feedback in the Holos reactor makes it less sensitive to low frequency reactivity oscillations.

The state-space model is next incorporated within a Model Predictive Control (MPC) algorithm for autonomous control. Several numerical results are presented to demonstrate a single-input–multiple-output and multiple-input–multiple-output control capability with the MPC. This is done for several assumed scenarios that incorporate flexible power operation requirements published by various organizations. The model and controller are then extended to include the dynamics of ^{135}Xe. With the ^{135}Xe dynamics we provide numerical results for daily load following operation that might be typical for a peaking plant to illustrate the importance of modeling all the essential physics for this type of operation. Figure EC.1 shows the results of the autonomous control algorithm for daily load following with explicit treatment of ^{135}Xe poisoning.

We also provide a comparative analysis of several control algorithms with the MPC. In this comparison, we use several other common control algorithms that have been previously studied for nuclear reactors. Specifically, we compare proportional-integral-derivative controllers, Linear-Quadratic regulators, and H_∞ controllers to MPC. Numerical comparisons for a particular scenario show that under ideal conditions each of these controllers can be made to be sufficiently accurate for the reactivity control problem. However, we make several arguments and provide some additional numerical results to show the superiority of MPC for this application.

From our results, a few near term activities are proposed to strengthen the analysis presented here. Additionally, we identify potential future tasks to build on this body of work. These activities largely focus on continuing to modernize, and advance the complexity of, the MPC algorithm explored so far. The work performed here will also serve as the basis of a consistent comparison with the passive reactivity control mechanisms that will be developed later in the project. We also wish to use the state-space model as a baseline for understanding what level of fidelity and accuracy this provides when compared to higher-fidelity models that will also be analyzed later in

this project. Finally, we wish to note some potential synergies with other Microreactor Program activities where the work performed here could be:

- used to extend the capabilities of the TRANSFORM library and broaden its application.
- leveraged in the MAGNET facility to provide control of the heaters in a way that is tunable so that the dynamic response of MAGNET and subsequent experimental data will be more representative of a particular reactor design.

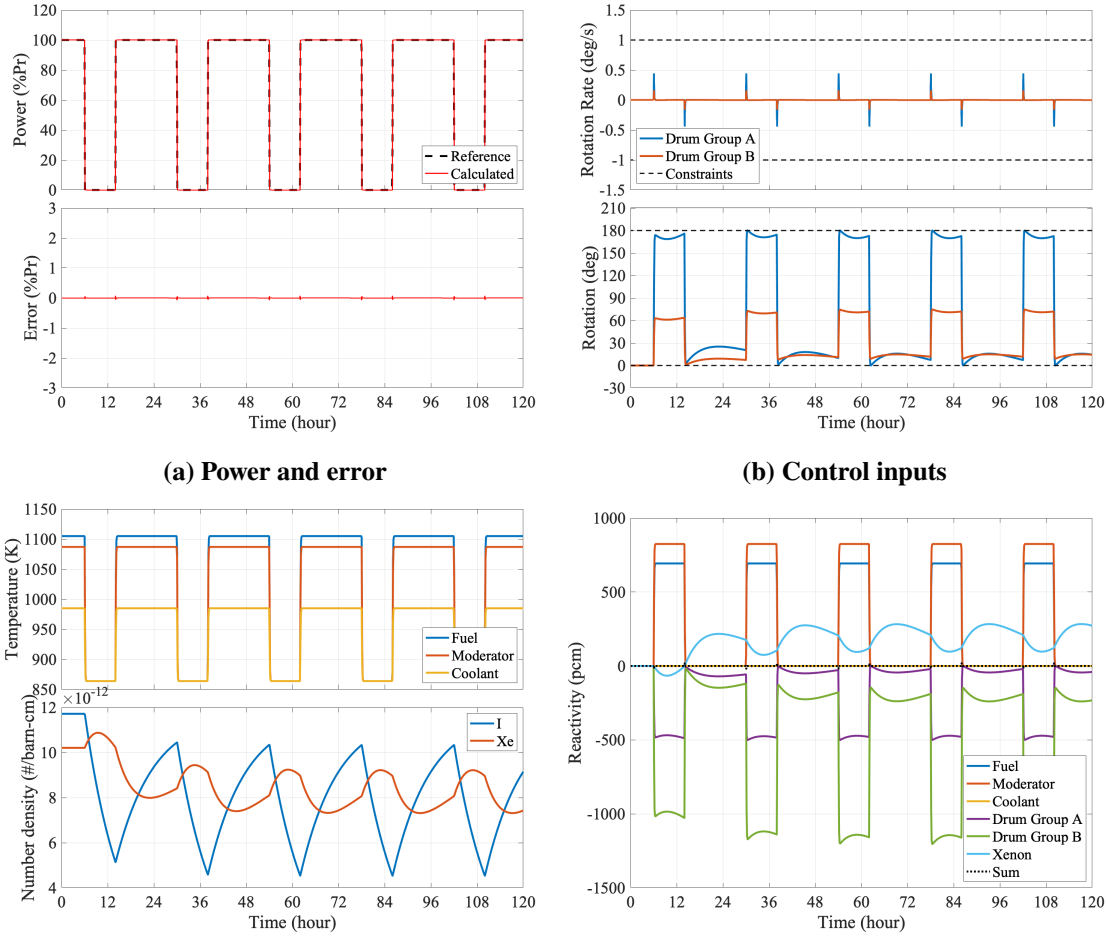

(a) Power and error

(b) Control inputs

(c) Temperature and density

(d) Reactivity change

Figure EC.1. Simulation Results for Daily Load Following

CONTENTS

LIST OF FIGURES

LIST OF TABLES

ACRONYMS

ANL Argonne National Laboratory

FPO Flexible Power Operation

HTGR High Temperature Gas Reactor

SAM Systems Analysis Module

SPM Subcritical Power Module

TH Thermal Hydraulics/Fluids

EUR European Utilities Requirements

MPC Model Predictive Control

PBMR Pebble Bed Modular Reactor

MAGNET Microreactor AGile Non-nuclear Experimental Testbed

LS-VHTR Liquid-Salt Very High Temperature Reactor

PID Proportional–Integral–Derivative

LQR Linear Quadratic Regulator

MIMO Multiple-Input and Multiple-Output

SIMO Single-Input and Multiple-Output

SISO Single-Input and Single-Output

PWR Pressurized Water Reactor

QP Quadratic Programming

1. INTRODUCTION

The overall aim of this project is to investigate and develop passive systems for autonomous control of High Temperature Gas Reactor (HTGR) special purpose reactors–or microreactors. In previous work [1], we investigated the reactivity of local temperature perturbations as one mode of physics for passive control, and variable reflector cross sections as the other.

In this report we document the development of a state-space dynamics model and control algorithms that may actively provide autonomous reactivity control of a microreactor–here our previous work provides the necessary coefficients for the state-space model.

The purpose of developing the state-space model and control algorithms is to provide a reference for how well existing control technologies will function given the task of reactivity control of a microreactor. These results will be used later in the project as the basis of a consistent comparison with the passive reactivity control mechanisms that will be developed. We also wish to use the state-space model as a baseline for understanding what level of fidelity and accuracy this provides when compared to higher-fidelity models that will be analyzed later in this project.

Many control algorithms exist, and have been applied to nuclear systems for the control of various components–including reactivity. While they have not been specifically investigated for microreactors, they have been investigated for countless other reactor designs. The most notable related applications are for space fission power systems as these reactor systems share many characteristics to microreactors; such as requiring a high degree of autonomy and being small in nature. Although, typically, space fission power systems have a smaller thermal output than microreactors. Consequently, the application of control algorithms to microreactor dynamics should not pose any significant additional challenges that have not already been encountered in the application of control algorithms of various other reactors.

In general, for autonomous control via the use of controllers based on conventional control algorithms and engineering, one requires real-time or faster than real-time methods. There are a few fundamentally different classes of algorithms that meet this requirement. In some control strategies, the reference signal of the controlled parameter is analyzed and controlled with some very general mathematical principles and formulations. A widely used example of this would be Proportional–Integral–Derivative (PID) controllers. The other class of algorithms use simple, real-time, models of the system dynamics as the basis of the control algorithm. A widely used, and state-of-the-art, example of model based control is Model Predictive Control (MPC). For the model based control approach one typically starts with a system of ordinary differential equations describing the dynamics of the system. These equations are linearized and transformed into a state-space representation. The state-space representation of the system dynamics is then used by the control algorithm and can also be used in conjunction with analytical tools to assess the stability of the system.

The detailed description, performance, and comparisons of modern control algorithms is the focus of this report. To begin, we proceed with some background on the reactor design that is the basis of the work performed here.

1.1 Background

As a specific use case for an HTGR, we use the reactor design under development by Holos. The Holos-Quad design is a scaled down HTGR with the core being composed of four SPMs. Each SPM is effectively an independent closed loop Brayton cycle power conversion unit with a nuclear heat source in a tube-shell heat exchanger configuration. This effectively eliminates the balance of plant. In earlier designs of this reactor the four SPMs were configurable so that they will create a critical reactor. An illustration of the SPM is shown in Fig. 1 A publicly available preliminary

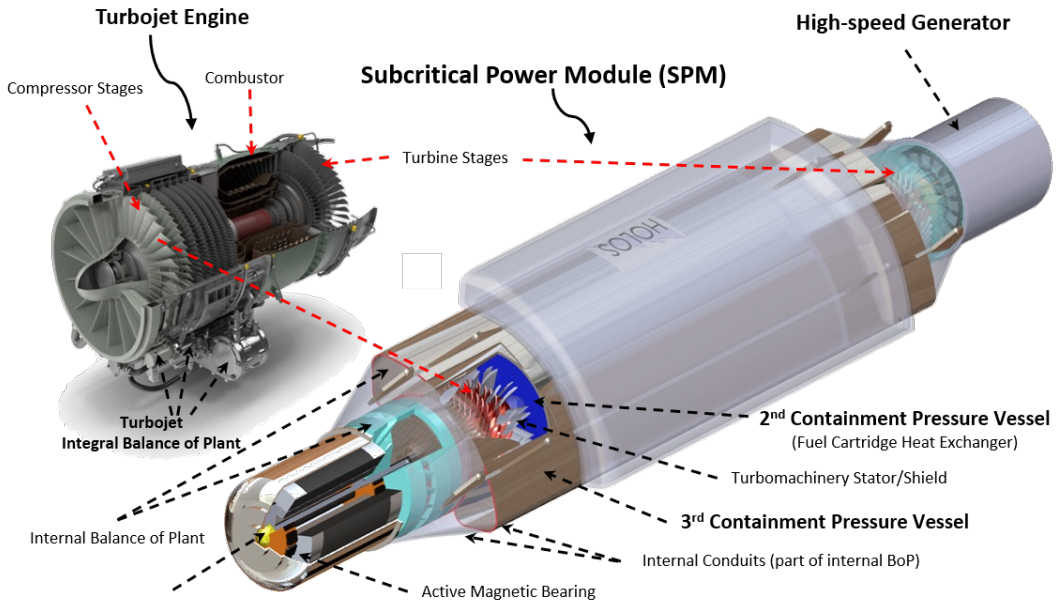

Figure 1. Illustration of an SPM as an Analogue to a Jet Engine

neutronic design of this reactor is described in [2]. The public design is illustrated in Fig. 2a with all SPMs inserted, and with SPMs separated in Fig. 2b.

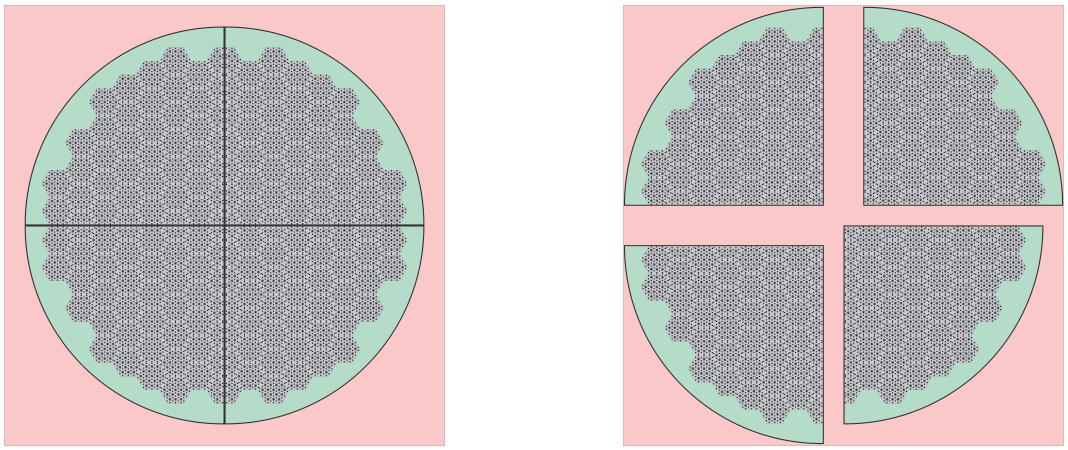

(a) Holos-Quad with SPMs together **(b) Holos-Quad with SPMs apart**

Figure 2. Preliminary Holos-Quad Design

However, since that time, the design has continued to evolve under the ARPA-E MEITNER program [3]. A new, proprietary design was developed by the ARPA-E Resource team at Argonne National Laboratory (ANL) and finalized on April 20th, 2020. This new design was reported in [4, 5]. The updated core design is the focus of the calculations and analysis of this report. In this reference design, the SPMs are still physically separated, but fixed in their quadrant, the SPMs are no longer actuated or moved to change reactivity. Additionally, there exists a central cruciform reflector between the SPMs for the shutdown control system. The final design with all drums in and out is pictured in Fig. 3.

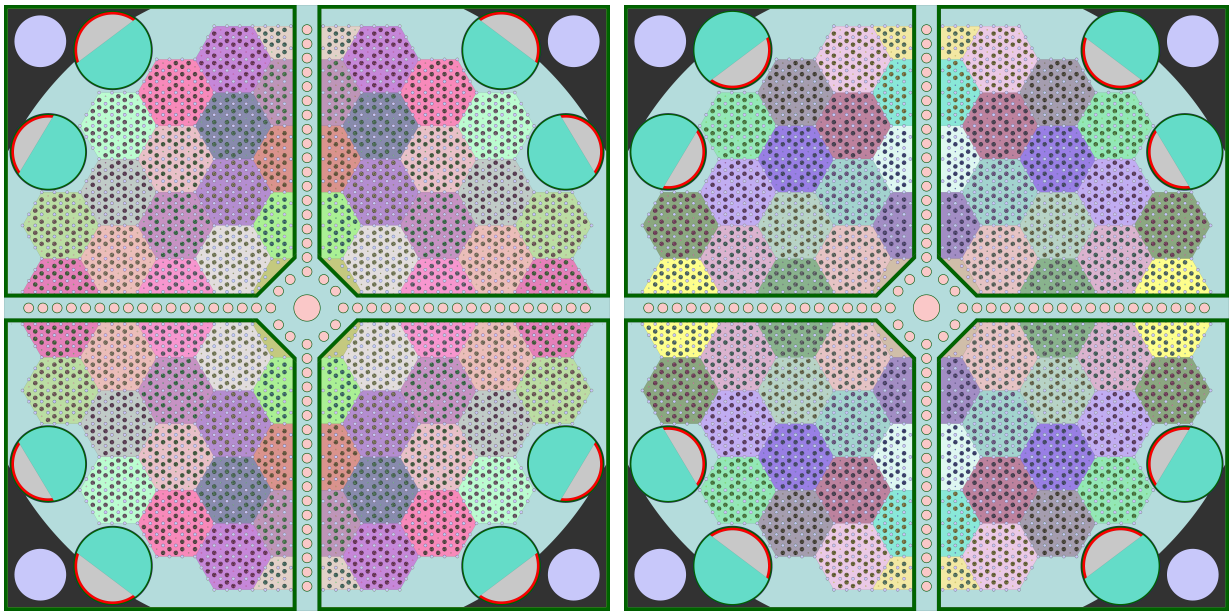

(a) Holos-Quad with Drums Out **(b) Holos-Quad with Drums In**

Figure 3. Preliminary Holos-Quad Control Drum Design

To assess the overall feasibility of the control algorithms, we consider several load following scenarios. For the power maneuvers considered here, we surveyed the literature for Flexible Power Operation (FPO) requirements. A summary of these requirements from various sources in terms of ramp rates and power ranges are given in Table 1 (reproduced from [1]). The various institutes suggest that the ramp rate should be in the range between $1\%P_r$/min and $20\%P_r$/min for FPO. Based on this data several contrived load follow sequences are developed to challenge the reactor dynamics model and control algorithms.

1.2 Organization of this Report

The remainder of this report is organized as follows: first we present the derivation of the state-space model and give the coefficients used in the analysis. Then, using the same model, we present a stability analysis, quantify the stability margin, and discuss some limitations of the state-space model. From our state-space model we next present how this used within the MPC algorithm. Numerical results are then presented for several load follow scenarios. Here we show the feasibility of MPC to provide an autonomous control capability, and the importance of including ^{135}Xe in the state-space representation when considering the daily load follow scenario. In the numerical results

Table 1. Summary of ramp rate requirements

Category	Ramp Rate ($\%P_r$/min)	Power Range Low / High ($\%P_r$)	Note
1	3 - 5	50 - 100	European Utilities Requirements (EUR) [6]
2	20	50 - 100	EUR, emergency [6]
3	5	50 - 100	USA, EPRI, INPO [7]
4	1	75 - 100	Belgium [7]
5	10	20 - 100	Germany, design limit [7]
6	10 5 2	80 - 100 50 - 100 20 - 100	Germany, operational limit [7]
7	10	0 - 100	Pebble Bed Modular Reactor (PBMR) [8]

we also perform a comparative study of various control algorithms as a basis for comparison with MPC and give some discussion. Finally we summarize our conclusions and note the on-going and future work of this project.

2. STATE-SPACE REPRESENTATION REACTOR DYNAMICS MODEL

In this report, we aim to develop numerical models for predictive control algorithms. To achieve this end, very simple computational models are required to meet the real-time calculation requirements. The numerical model is composed of the point kinetics model and a three-temperature Thermal Hydraulics/Fluids (TH) model. The models are developed to represent the reactor behavior of the Holos-quad reactor.

2.1 Reactor Kinetics Model

To model the time-dependent behavior of the reactor, we use the standard point kinetics equations with 6 delayed groups and component reactivity feedback. These equations are given as:

$$\frac{dn(t)}{dt} = \frac{\rho(t) - \beta}{\Lambda} n(t) + \sum_{i=1}^{m} \lambda_i C_i(t), \tag{1}$$

$$\frac{dC_i(t)}{dt} = \frac{\beta_i}{\Lambda} n(t) - \lambda_i C_i(t) \ , \quad i = 1, 2, ..., m = 6, \tag{2}$$

where n is the neutron density; m is the number of delayed groups; ρ is the reactivity; β is the total effective delayed neutron fraction; β_i is the i-th group effective delayed neutron fraction; λ_i is the i-th group effective delayed neutron precursor decay constant; Λ is the generation time; and C_i is the i-th group precursor concentration.

The initial condition of the precursor concentration at steady-state is derived by setting the left side of Eq. (2) to be zero as follows:

$$C_{i0} = \frac{\beta_i n_0}{\lambda_i \Lambda}, \quad i = 1, 2, ..., m, \tag{3}$$

where the subscript 0 denotes the initial steady-state condition.

Using Eq. (3), the normalized point kinetics equations are written as follow:

$$\frac{d\bar{n}(t)}{dt} = \frac{\rho(t) - \beta}{\Lambda}\bar{n}(t) + \sum_{i=1}^{m} \frac{\beta_i}{\Lambda}\bar{C}_i(t), \tag{4}$$

$$\frac{d\bar{C}_i(t)}{dt} = \lambda_i \bar{n}(t) - \lambda_i \bar{C}_i(t), \quad i = 1, 2, ..., m, \tag{5}$$

where $\bar{n}(t)$is $n(t)/n_0$, and $\bar{C}_i(t)$ is $C_i(t)/C_{i0}$. The non-dimensional normalized forms facilitate the stability analysis and use within a control algorithm.

The reactivity feedback model has the components for reactivity due to the control systems and passive feedback mechanisms. The Holos reactor has two ways to actively control reactivity. One is through the rotation of some combination of the control drums simultaneously. The other is by moving one the SPMs, however, as was shown in [9], the reactivity is far too sensitive to this mechanism, and thus should only be used for transport or emergency shutdown. Further, the design was modified to eliminate this feature because of the sensitivity. Therefore, in this study, the control drum is the primary reactivity control mechanism considered. The reactivity model with the control drum and the various temperature feedback mechanisms is defined as follows:

$$\delta\rho(t) = \alpha_f \delta T_f(t) + \alpha_m \delta T_m(t) + \alpha_c \delta T_c(t) + \delta\rho_d(t), \tag{6}$$

$$\frac{d\delta\rho_d(t)}{dt} = G_d Z_d(t), \tag{7}$$

where $\delta\rho_d$ is the reactivity change due to control system (drums); α_f is the reactivity coefficient of fuel; α_m is the reactivity coefficient of moderator; α_c is the reactivity coefficient of coolant; and $\delta T_f(t)$, $\delta T_m(t)$, and $\delta T_c(t)$ are the temperature changes of the fuel, moderator, and coolant, respectively. G_d is the differential reactivity worth of the control drums; and Z_d is the velocity of the control drum.

Eqs. (6) and (7) are derived for the Single-Input and Single-Output (SISO) case which means that only one type of control mechanism is used for the control of the power level. However, Holos has 8 control drums that can be adjusted separately. If it is necessary to use multiple-inputs to maneuver the power, then some additional elements should be added to Eq. (6). Only one control input is used in the derivations of MPC and the state-space model for simplicity, however, treating the different drums as multiple inputs/outputs is straightforward.

The kinetics parameters and the reactivity coefficients used in the model are listed in Table 2. These come from various references which are documented in [9] and also from the calculations described in [1].

Table 2. Coefficients of Reactor Dynamics Model

Parameter	Value	Unit	Parameter	Value	Unit
β	480.10	pcm	α_f	-2.875	pcm/K
β_1	14.20	pcm	α_m	-3.696	pcm/K
β_2	92.40	pcm	α_c	0.000	pcm/K
β_3	78.00	pcm	c_f	977.00	J/kg/K
β_4	206.60	pcm	c_m	1697.00	J/kg/K
β_5	67.10	pcm	c_c	5188.60	J/kg/K
β_6	21.80	pcm	m_f	2002.00	kg
Λ	0.00168	s	m_m	11573.00	kg
λ_1	0.01270	1/s	m_c	500.00	kg
λ_2	0.03170	1/s	$\dot{m}_c$	17.50	kg/s
λ_3	0.11600	1/s	T_{f0}	1105	K
λ_4	0.31100	1/s	T_{m0}	1087	K
λ_5	1.40000	1/s	T_{in0}	864	K
λ_6	3.87000	1/s	T_{out0}	1106	K
n_0	2.25E+13	m^{-3}	K_{fm}	1.17E+06	W/K
P_r	22.00	MW	K_{mc}	2.16E+05	W/K
q	0.96	-	-	-	-

Table 3. Reactivity worth of control drums

# of control drums	Differential reactivity worth (pcm/deg)
1	-2.78
2	-7.33
4	-16.11
8	-26.11

2.2 Three-Temperature Thermal-Fluids Model

For the thermal-fluids dynamics, we consider the 3-temperature model of a point reactor–which should be reasonable for the slow transients studied here. Validation against the Systems Analysis Module (SAM) code is a future activity. We treat the heat-balance equations of the fuel, moderator and coolant temperatures separately as:

$$m_f c_f \frac{dT_f(t)}{dt} = qP_r\bar{n}(t) - K_{fm}\left(T_f(t) - T_c(t)\right), \tag{8}$$

$$m_m c_m \frac{dT_m(t)}{dt} = (1-q)\,P_r\bar{n}(t) + K_{fm}\left(T_f(t) - T_m(t)\right) - K_{mc}\left(T_m(t) - T_c(t)\right), \tag{9}$$

$$m_c c_c \frac{dT_c(t)}{dt} = K_{mc}\left(T_m(t) - T_c(t)\right) - 2\dot{m}_c c_c\left(T_c(t) - T_{in}\right), \tag{10}$$

where P_r is the rated power of reactor; the dimensionless parameter q represents the fraction of heat deposited in the fuel (the rest being deposited in the moderator); m_f, m_m, and m_c are the masses of fuel, moderator, and coolant, respectively; $\dot{m}_c$ is the coolant flow rate; c_f, c_m, and c_c

are the heat capacities of the fuel, moderator, and coolant, respectively; K_{fm} and K_{mc} are the heat transfer coefficients from fuel to moderator, and from moderator to coolant, respectively; and T_{in} is the inlet coolant temperature.

The global heat transfer coefficients can be calculated directly based on their physical definitions with some approximation for the geometry.. However, we used an alternative approach. Using the steady-state equations, we may express the coefficients as:

$$K_{fm} = \frac{qP_r}{T_{f0} - T_{m0}}, \tag{11}$$

$$K_{mc} = \frac{P_r}{T_{m0} - T_{c0}}, \tag{12}$$

where $T_{c0} = (T_{in0} + T_{out0})/2$ is the nominal average coolant temperature.

Using SAM, the steady-state temperatures were calculated, and from this solution the heat transfer coefficients were calculated based on Eqs. (11) and (12). These values with the remaining thermal-fluids parameters are also listed in Table 2.

2.3 State-Space Reactor Model Description

We now wish to obtain the reactivity response that couples the reactor kinetics and TH dynamics equations. To accomplish this, we formulate a time-dependent control problem. This begins with converting the mathematical models for the normalized point kinetics, reactivity, and thermal-fluids into a state-space model. The neutron density is first written in the following *deviation* form:

$$\frac{d\delta\bar{n}(t)}{dt} = \frac{1}{\Lambda}\delta\rho(t) - \frac{\beta}{\Lambda}\delta\bar{n}(t) + \sum_{i=1}^{m}\frac{\beta_i}{\Lambda}\delta\bar{C}_i(t), \tag{13}$$

where the symbol δ indicates the deviation of a variable from an equilibrium value, i.e. $x(t) = x_0 + \delta x(t)$.

In Eq. (13), $\bar{n}_0$ is omitted since it is equal to 1. Inserting Eq. (6) into Eq. (13) leads to:

$$\frac{d\delta\bar{n}(t)}{dt} = -\frac{\beta}{\Lambda}\delta\bar{n}(t) + \sum_{i=1}^{m}\frac{\beta_i}{\Lambda}\delta\bar{C}_i(t) + \frac{1}{\Lambda}\left(\alpha_f\delta T_f(t) + \alpha_m\delta T_m(t) + \alpha_c\delta T_c(t) + \delta\rho_d(t)\right). \tag{14}$$

In a similar way, the equations for the precursor density, fuel temperature, moderator temperature, and coolant temperature can be written as follows:

$$\frac{d\delta\bar{C}_i(t)}{dt} = \lambda_i\delta\bar{n}(t) - \lambda_i\delta\bar{C}_i(t), \tag{15}$$

$$\frac{d\delta T_f(t)}{dt} = \frac{qP_r}{m_f c_f}\delta\bar{n}(t) - \frac{K_{fm}}{m_f c_f}\left(\delta T_f(t) - \delta T_m(t)\right), \tag{16}$$

$$\frac{d\delta T_m(t)}{dt} = \frac{1-q}{m_m c_m}P_r\delta\bar{n}(t) + \frac{K_{fm}}{m_m c_m}\left(\delta T_f(t) - \delta T_m(t)\right) - \frac{K_{mc}}{m_m c_m}\left(\delta T_m(t) - \delta T_c(t)\right), \tag{17}$$

$$\frac{d\delta T_c(t)}{dt} = \frac{K_{mc}}{m_c c_c}\left(\delta T_m(t) - \delta T_c(t)\right) - \frac{2\dot{m}_c c_c}{m_c c_c}\delta T_c(t). \tag{18}$$

Neglecting the higher-order terms in Eqs. (14) to (18) (e.g. linearizing the equations), we can now express them in the following state-space model form:

$$\left\{\begin{aligned}\dot{\mathbf{x}}_\mathbf{c} &= \mathbf{A_c}\mathbf{x_c} + \mathbf{B_c}\mathbf{u}\\ \mathbf{y} &= \mathbf{C_c}\mathbf{x_c}\end{aligned}\right\}, \tag{19}$$

where the system matrix, $\mathbf{A_c}$, is

$$\mathbf{A_c} = \begin{bmatrix} -\frac{\beta}{\Lambda} & \frac{\beta_1}{\Lambda} & \cdots & \frac{\beta_m}{\Lambda} & \frac{\alpha_f}{\Lambda} & \frac{\alpha_m}{\Lambda} & \frac{\alpha_c}{\Lambda} & \frac{1}{\Lambda} \\ \lambda_1 & -\lambda_1 & \cdots & 0 & 0 & 0 & 0 & 0 \\ \vdots & \vdots & \vdots & \vdots & \vdots & \vdots & \vdots & \vdots \\ \lambda_m & 0 & \cdots & -\lambda_m & 0 & 0 & 0 & 0 \\ \frac{qP_r}{m_f c_f} & 0 & \cdots & 0 & -\frac{K_{fm}}{m_f c_f} & \frac{K_{fm}}{m_f c_f} & 0 & 0 \\ \frac{(1-q)P_r}{m_m c_m} & 0 & \cdots & 0 & \frac{K_{fm}}{m_m c_m} & -\frac{K_{fm}+K_{mc}}{m_m c_m} & \frac{K_{mc}}{m_m c_m} & 0 \\ 0 & 0 & \cdots & 0 & 0 & \frac{K_{mc}}{m_c c_c} & -\frac{K_{mc}+2\dot{m}_c c_c}{m_c c_c} & 0 \\ 0 & 0 & \cdots & 0 & 0 & 0 & 0 & 0 \end{bmatrix}, \tag{20}$$

and the state vector, $\mathbf{x_c}$, is

$$\mathbf{x_c} = \begin{bmatrix} \delta\bar{n}(t) & \delta\bar{C}_1(t) & \cdots & \delta\bar{C}_m(t) & \delta T_f(t) & \delta T_m(t) & \delta T_c(t) & \delta\rho_d(t) \end{bmatrix}^T. \tag{21}$$

The input matrix, $\mathbf{B_c}$, is

$$\mathbf{B_c} = \begin{bmatrix} 0 & 0 & \cdots & 0 & 0 & 0 & 0 & G_d \end{bmatrix}^T, \tag{22}$$

and the control vector, $\mathbf{u}$, and output vector, $\mathbf{y}$, are

$$\mathbf{u} = \left[Z_d(t)\right], \tag{23}$$

and

$$\mathbf{y} = \left[\delta\bar{n}(t)\right], \tag{24}$$

respectively. Finally the output matrix, $\mathbf{C_c}$, is:

$$\mathbf{C_c} = \begin{bmatrix} 1 & 0 & \cdots & 0 & 0 & 0 & 0 & 0 \end{bmatrix}. \tag{25}$$

Once again, these matrices and vectors are written for a SISO problem. If it is necessary to solve a multiple-input problem, additional columns and rows should be added to Eqs. (22) and (23), respectively. Similarly, Eqs. (24) and (25) are defined for a single-output case. A multiple-output problem can be made by adding additional rows into Eqs. (24) and (25).

2.4 State-Space Model with ^{135}Xe

In Sections 2.1 and 2.3, the linearized state-space model was developed from the point kinetics and three-temperature model equations. This is typical in much of the literature for reactor control analysis as these works tend to consider short time scales where ^{135}Xe dynamics are negligible. However, the ^{135}Xe buildup is very important for daily load following operation. To account for this type of load following operation, the ^{135}Xe and ^{135}I models are added as additional terms in the component reactivity feedback model (Eq. (6)). The first order dynamics of ^{135}Xe are illustrated by the decay chain shown in Fig. 4.

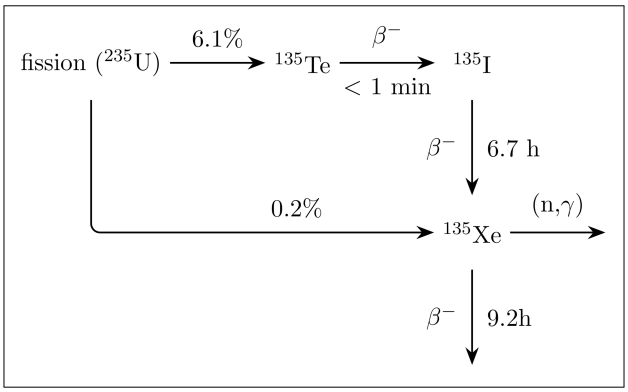

Figure 4. ^{135}Xe yield

Based on Fig. 4, the ^{135}Xe absorption is proportional to both the ^{135}Xe concentration and the neutron flux $\phi(t)$. The differential equations for the ^{135}I and ^{135}Xe concentrations are:

$$\frac{dI(t)}{dt} = \gamma_I \Sigma_f v n_0 \bar{n}(t) - \lambda_I I(t), \tag{26}$$

$$\frac{dX(t)}{dt} = \gamma_X \Sigma_f v n_0 \bar{n}(t) + \lambda_I I(t) - \lambda_X X(t) - \sigma_X v n_0 \bar{n}(t) X(t), \tag{27}$$

where γ_I and γ_X are the fission yields of ^{135}I and ^{135}Xe, respectively; v is the average velocity of the thermal neutrons; λ_I and λ_X are the radioactive decay rates of ^{135}I and ^{135}Xe, respectively; and σ_X is the microscopic absorption cross section of ^{135}Xe.

The reactivity model with ^{135}Xe is defined as follows:

$$\begin{aligned}\delta\rho(t) &= \delta\rho_d(t) + \alpha_f \delta T_f(t) + \alpha_m \delta T_m(t) + \alpha_c \delta T_c(t) - \delta\rho_X(t) \\ &= \delta\rho_d(t) + \alpha_f \delta T_f(t) + \alpha_m \delta T_m(t) + \alpha_c \delta T_c(t) - \frac{\sigma_X}{\Sigma_a + DB^2}\delta X(t),\end{aligned} \tag{28}$$

where ρ_X is the ^{135}Xe reactivity [10]; Σ_a is the macroscopic absorption cross section; and DB^2 represents the neutron leakage from the reactor. The term $\Sigma_a + DB^2$ is therefore, the total loss of neutrons driven by absorption and leakage. The term $-\sigma_X/(\Sigma_a + DB^2)$ can be interpreted as the ^{135}Xe coefficient of reactivity. Note that $\Sigma_a + DB^2 = \nu\Sigma_f$ for the critical reactor.

Inserting Eq. (28) into Eq. (13) leads to:

$$\begin{aligned}\frac{d\delta\bar{n}(t)}{dt} &= -\frac{\beta}{\Lambda}\delta\bar{n}(t) + \sum_{i=1}^{m}\frac{\beta_i}{\Lambda}\delta\bar{C}_i(t) - \sigma_X v\delta X(t) \\ &+ \frac{1}{\Lambda}\left(\alpha_f\delta T_f(t) + \alpha_m\delta T_m(t) + \alpha_c\delta T_c(t) + \delta\rho_d(t)\right),\end{aligned} \tag{29}$$

because the neutron generation time $\Lambda = 1/v\left(\Sigma_a + DB^2\right)$.

The deviation forms of the ^{135}I and ^{135}Xe equations are

$$\frac{d\delta I(t)}{dt} = \gamma_I\Sigma_f v n_0\delta\bar{n}(t) - \lambda_I\delta I(t), \tag{30}$$

$$\frac{d\delta X(t)}{dt} = \left(\gamma_X\Sigma_f - \sigma_X X_0\right)v n_0\delta\bar{n}(t) + \lambda_I\delta I(t) - \left(\lambda_X + \sigma_X v n_0\right)\delta X(t). \tag{31}$$

Eqs. (30) and (31) have initial values n_0 for the neutron population and X_0 for the ^{135}Xe concentration. These parameters are defined as follow:

$$n_0 = \frac{P_r}{\epsilon} = \frac{P_r}{\int_V \kappa\Sigma_f v dV}, \tag{32}$$

$$I_0 = \frac{\gamma_i\Sigma_f v n_0}{\lambda_i}, \tag{33}$$

$$X_0 = \frac{\gamma_x\sigma_f v n_0 + \lambda_i I_0}{\lambda_x + \sigma_x v n_0}, \tag{34}$$

where κ is the energy per fission deposited in fuel, and ϵ represents the power per unit neutron density.

Equations (15) to (18) and (29) to (31) are written in the state-space model form (i.e. Eq. (19)) in a manner similar to Section 2.3. In this case, the system matrix $\mathbf{A_c}$ and the state vector $\mathbf{x_c}$ are now defined as follows:

$$\mathbf{A_c} = \begin{bmatrix}
-\frac{\beta}{\Lambda} & \frac{\beta_1}{\Lambda} & \cdots & \frac{\beta_m}{\Lambda} & \frac{\alpha_f}{\Lambda} & \frac{\alpha_m}{\Lambda} & \frac{\alpha_c}{\Lambda} & 0 & -\sigma_x v & \frac{1}{\Lambda} \\
\lambda_1 & -\lambda_1 & \cdots & 0 & 0 & 0 & 0 & 0 & 0 & 0 \\
\vdots & \vdots & \vdots & \vdots & \vdots & \vdots & \vdots & \vdots & \vdots & \vdots \\
\lambda_m & 0 & \cdots & -\lambda_m & 0 & 0 & 0 & 0 & 0 & 0 \\
\frac{qP_r}{m_f c_f} & 0 & \cdots & 0 & -\frac{K_{fm}}{m_f c_f} & \frac{K_{fm}}{m_f c_f} & 0 & 0 & 0 & 0 \\
\frac{(1-q)P_r}{m_m c_m} & 0 & \cdots & 0 & \frac{K_{fm}}{m_m c_m} & -\frac{K_{fm}+K_{mc}}{m_m c_m} & \frac{K_{mc}}{m_m c_m} & 0 & 0 & 0 \\
0 & 0 & \cdots & 0 & 0 & \frac{K_{mc}}{m_c c_c} & -\frac{K_{mc}+2\dot{m}_c c_c}{m_c c_c} & 0 & 0 & 0 \\
\gamma_i\sigma_f v n_0 & 0 & \cdots & 0 & 0 & 0 & 0 & -\lambda_i & 0 & 0 \\
\left(\gamma_x\Sigma_f - \sigma_x X_0\right)v n_0 & 0 & \cdots & 0 & 0 & 0 & 0 & -\lambda_i & -\lambda_x - \sigma_x v n_0 & 0 \\
0 & 0 & \cdots & 0 & 0 & 0 & 0 & 0 & 0 & 0
\end{bmatrix}, \tag{35}$$

$$\mathbf{x_c} = \left[\begin{array}{ccccccccc} \delta\bar{n}(t) & \delta\bar{C}_1(t) & \cdots & \delta\bar{C}_m(t) & \delta T_f(t) & \delta T_m(t) & \delta T_c(t) & \delta I(t) & \delta X(t) & \delta\rho_d(t) \end{array} \right]^T. \quad (36)$$

The input matrix $\mathbf{B_c}$, control vector $\mathbf{u}$, output vector $\mathbf{y}$, and output matrix $\mathbf{C_c}$ can be defined in a similar manner as Section 2.3.

3. STABILITY ANALYSIS OF THE STATE-SPACE MODEL

Prior to developing a control algorithm, the linear stability of the system should be studied. The reason for this is to characterize the overall physical stability of the system without control. If the system has inherently unstable points of operation, then the control algorithm must account for this. Further, it provides a baseline assessment of the system's dynamic response without control, and this allows one to verify that adding a controller does not lead to an unstable system.

The linear stability analysis can be performed by one of several approaches, all yielding the response of the system to small perturbations around the steady-state equilibrium condition. If such perturbations decay, and the system returns to an equilibrium condition, the system is linearly stable. However, if these perturbations grow, the system is said to be linearly unstable.

It is important to note that a system which is linearly unstable, will not necessarily diverge when small perturbations are applied. This is because when the perturbations grow, nonlinear terms become significant and can no longer be neglected. In some cases the nonlinear terms can converge the dynamics into a steady limit cycle, such that the dynamics will show bounded oscillations. Alternatively, the nonlinear terms can drive the system to an unstable behavior. For our present scope, we limit our analysis to linear stability. Although later in this section we attempt to quantify the limits of the validity of the linear stability analysis.

A powerful method to study linear stability is performed in the frequency domain by analyzing the transfer function of the system. This function, $G(s)$, is defined as the ratio between the output and the input in the Laplace domain. A graphical representation of the transfer function is typically illustrated with a Bode diagram. This diagram shows the response of the reactor in terms of its *gain* and *phase* to external perturbations of different frequencies. Bode diagrams are frequently used to analyze the stability margins of the system. Their primary advantage is the characterization of the system dynamics over the full frequency domain without having to perform numerous, potentially expensive, numerical calculations. Additionally, by analyzing the poles of the transfer function, within the formalism of the root locus method, the linear stability for varying power levels can also be analyzed.

In this section we derive the closed-loop transfer function and discuss the reactor response and stability in terms of its Bode diagram and the root locus method.

3.1 Closed-loop Transfer Function

Derivation of the transfer function of linear (or linearized in our case) dynamical systems is performed in the Laplace domain. To begin, we start from the state-space model derived in Section 2.3 (Eqs. (19) to (24)) that excludes the ^{135}Xe dynamics. This is done for simplicity; the derivation will be expanded in the future to include ^{135}Xe.

We apply the Laplace transform on these equations to convert them into the s domain. Recalling

that $\mathcal{L}\left[df/dt\right] = sf(s) - s_0$, the system of differential equations are transformed to a system of algebraic equations that we may then solve analytically. The Laplace transformation of Eqs. (19) to (24) yields:

$$s\delta\bar{n}(s) = -\frac{\beta}{\Lambda}\delta\bar{n}(s) + \frac{\delta\rho(s)}{\Lambda} + \sum_{i=1}^{6}\lambda_i\delta\bar{C}_i(s), \tag{37}$$

$$s\delta\bar{C}_i(s) = \frac{\beta_i}{\Lambda}\delta\bar{n}(s) - \lambda_i\delta\bar{C}_i(s), \tag{38}$$

$$m_f c_f s\delta T_f(s) = qP_r\delta\bar{n}(s) - K_{fm}\delta T_f(s) + K_{fm}\delta T_m(s), \tag{39}$$

$$m_m c_m s\delta T_m(s) = (1-q)\delta P_r(s) + K_{fm}\delta T_f(s) - (K_{fm} + K_{mc})\delta T_m(s) + K_{mc}\delta T_c(s), \tag{40}$$

$$m_c c_c s\delta T_c(s) = K_{mc}\delta T_m(s) - (K_{mc} + 2\dot{m}_c c_c)\delta T_c(s), \tag{41}$$

In the Laplace domain the linear system is represented by the block diagram in Fig. 5. The well

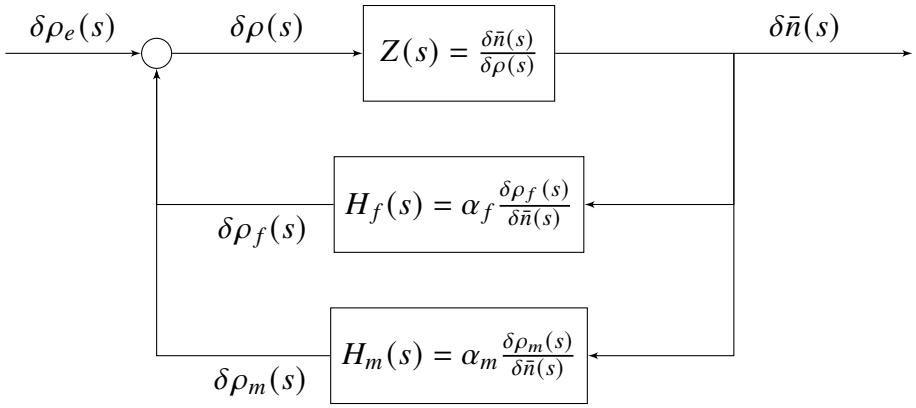

Figure 5. Block diagram of the state-space model with an external reactivity perturbation and reactivity feedback from the fuel and moderator temperatures.

known zero-power transfer function is derived using Eqs. (37) and (38):

$$Z(s) = \frac{1}{s}\left(\Lambda + \sum_{i=1}^{6}\frac{\beta_i}{s+\lambda_i}\right)^{-1}. \tag{42}$$

Using Eqs. (39) to (41) we can find the transfer functions of the fuel and moderator feedback as:

$$H_f(s) = \frac{\alpha_f P_r\bar{n}_0}{D}\left[(K_{mc} + 2\dot{m}_c c_c + m_c c_c s)\left(K_{fm} + qm_m c_m s\right) + qK_{mc}\left(2\dot{m}_c c_c + m_c c_c s\right)\right], \tag{43}$$

$$H_m(s) = \frac{\alpha_m P_r\bar{n}_0}{D}\left[(K_{mc} + 2\dot{m}_c c_c + m_c c_c s)\left(K_{fm} + (1-q)m_f c_f s\right)\right], \tag{44}$$

where the denominator D is defined as:

$$\begin{aligned} D \equiv\ & K_{mc}(K_{fm} + m_f c_f s)(2\dot{m}_c c_c + m_c c_c s) \\ & + (K_{mc} + 2\dot{m}_c c_c + m_c c_c s)\left(K_{fm}(m_f c_f s + m_m c_m s) + m_f c_f m_m c_m s^2\right). \end{aligned} \tag{45}$$

Based on the block diagram description in Fig. 5, the closed-loop transfer function is:

$$G(s) = \frac{Z(s)}{1 - \left(H_f(s) + H_m(s)\right) Z(s)}. \tag{46}$$

As explained above, a graphical representation of the transfer function can be expressed in the formalism of the Bode diagram. In this method, the function is projected into the frequency domain by using $G(s) \rightarrow G(i\omega)$. The gain and phase of this complex function can now be plotted, showing the amplitude gain of the system and the phase difference between the input and output signals, respectively.

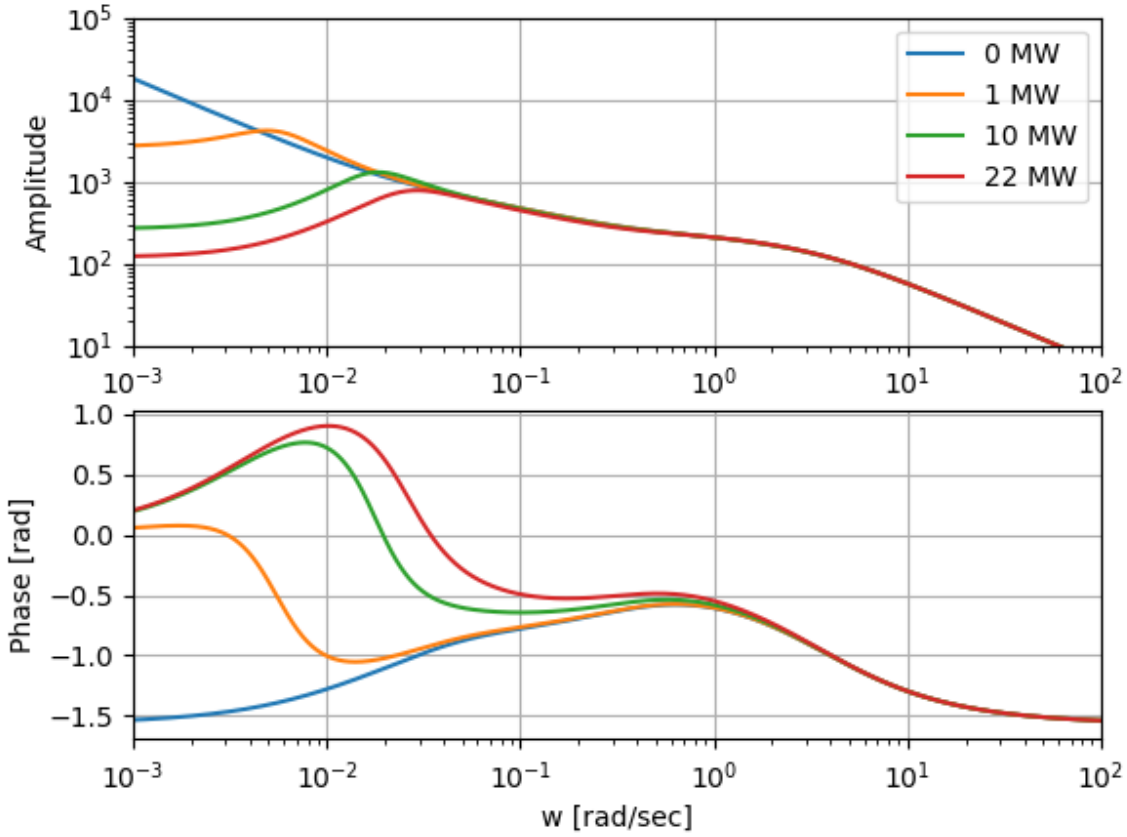

Figure 6. Bode diagram of the state-space model for increasing power levels. Both magnitude (upper panel) and phase (lower panel) depicted.

The Bode diagram of the state-space model is depicted in Fig. 6 for increasing power levels, from zero up to the nominal power. For zero-power, the familiar zero-power transfer function is obtained, which shows a monotonically decreasing behaviour in the Bode magnitude plot. Recall that the response of the system under zero-power conditions is driven solely by the delayed neutrons. Thus, we observe in this case, that high frequency reactivity oscillations do not lead to any significant gain in the reactivity output. However, for low frequency reactivity oscillations, there is reactivity gain

as the multiplication of the system may be increased through super-position of the delayed neutron emitters from successive reactivity oscillations. Naturally, as power increases, the temperature reactivity feedback begins to play a role. Since both the fuel and moderator feedback are negative they dampen the external perturbations. Here this is evident for the low-frequency oscillations because of the thermal time constants related to the conduction and heat capacity of graphite.

Another interesting observation comes from the phase behavior. For the zero-power reactor, the phase is always negative. This means that the input reactivity oscillations are lagging behind the power output. However, when the power level increases, the phase becomes positive for low frequencies. Here, due to the time scales of the feedback, the power response lags behind the reactivity input.

The use of the Bode diagram also enables us to study uncertainties regarding the nominal values used in this study. To explore this, we studied the dependence of the Bode plot to changes of ±50% in each of the nominal values given in Table 2. For many of the parameters this is an extremely large range to consider, thus we presume that this range would bound most viable HTR-like microreactor designs.

Figure 7 illustrates the range in the Bode diagram for changes in α_f and m_m. For the other coefficients, the overall effect of the ±50% uncertainty did not produce a significant change in the Bode diagram. As α_f increases, gain damping is also increased, due to the stronger negative feedback. Changes in the frequency response are also observed for different values of the moderator mass (m_m). In this respect, the large graphite mass acts as a thermal buffer that delays the reactivity response of the fuel, hence the moderator mass changes affect the frequency response. The frequency dependence on m_m is found to be significantly larger compared to changes in the fuel mass (m_f) or coolant mass (m_c). We believe this is explained by the large differences between the nominal values of these parameters.

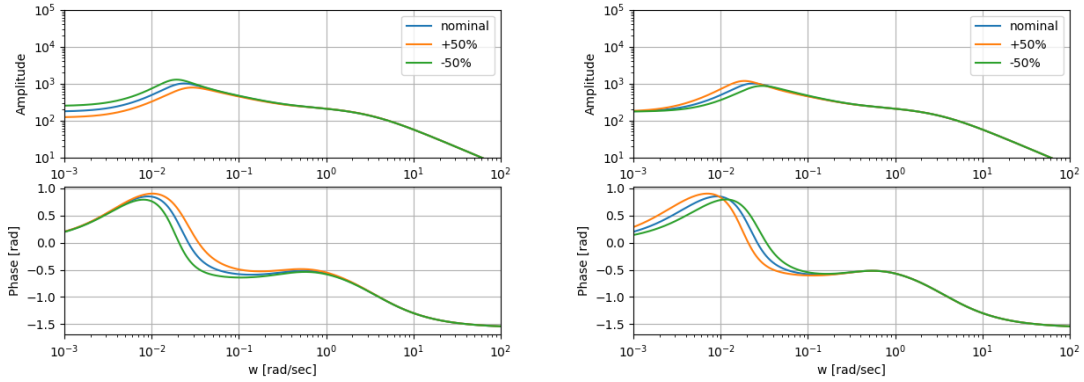

(a) α_f **(b)** m_m

Figure 7. Bode plot for ±50% change in nominal values of (a) α_f and (b) m_m.

3.2 Linear Stability Analysis

In a previous study, a simplified state-space model of an HTR-like microreactor was used to study linear stability using the Routh-Hurwitz method [11]. The simplified model includes only two

temperature variables, namely fuel and moderator. The parameter values were based on the Holos-Quad design. The study showed that the dynamics is linearly stable for a wide range of operational parameters. In addition, it showed that an unstable dynamics may theoretically occur even when both reactivity coefficients (fuel and moderator) are negative, however it requires a very small and nonphysical magnitude of the fuel coefficient of reactivity.

For our present work, we study the linear stability of the three-temperature model. Having derived the transfer function in the previous subsection, we use a different approach for stability study here, namely the root locus method. In this method, the poles of the transfer function are depicted in the Laplace s-plane. If all poles have a negative real part (i.e. located in the negative half-plane), the system is linearly stable. However, if any of the poles have a positive real value, the system is linearly unstable. Note that, based on Eq. (46), the poles of the transfer function are the roots of $1 - \left(H_f(s) + H_m(s)\right) Z(s)$.

The root locus diagram of the state-space model is depicted in Fig. 8 for increasing power levels. As shown in the figure, there exists more than one pole to the transfer function. However, all poles have a negative real component. Moreover, the magnitude of the real part increases with power becoming small; this is attributed to the negative nature of the reactivity feedback mechanisms. We therefore conclude that the system is linearly stable, and it becomes even more stable as power increases due to the stabilizing feedback mechanisms.

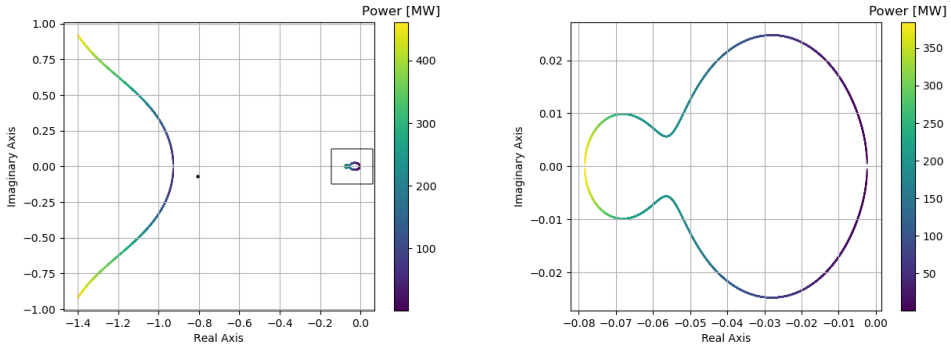

(a) **(b)**

Figure 8. Root locus stability diagram, depicted for increasing power levels. The rectangle area in (a) is magnified in (b).

This result can be compared with a recent stability analysis performed for the Liquid-Salt Very High Temperature Reactor (LS-VHTR) reactor [12], a prismatic liquid salt-cooled, graphite moderated high-temperature reactor. In that work, a similar three-temperature state-space model was used, and the linear stability was also analyzed using the root locus method. The study showed that the LS-VHTR is also linearly stable for the operational range of parameters. Comparison of the two root locus diagrams shows that, in both the Holos-Quad and LS-VHTR models, the most positive pole of the transfer function becomes more negative as the power increases. However, there are some qualitative differences between the root locus diagrams of the two models; specifically, the shape of the roots near zero (depicted in Fig. 8b). Since the power of the LS-VHTR reactor is significantly higher (2.4 GWt) than the microreactor, the mass of graphite and coolant flow rate are

also significantly higher. We conclude that these differences may be attributed as the cause of the differences in the root locus diagrams.

3.3 Limitations of the Linearized Model

The derivation of linearized model presented above is based on the assumption that small deviations from steady-state are introduced. Accordingly, the high-order terms ($\delta n(t)\delta\rho(t)$ and $\delta n(t)\delta X(t)$) are neglected. Through simulations performed in the time-domain that include and exclude the higher-order terms, it is possible to quantify the effect of neglecting the higher-order terms. Considering the nonlinear term involving the flux and ^{135}Xe we have:

$$\begin{aligned} n(t)X(t) &= (n_0 + \delta n(t))(X_0 + \delta X(t)) \\ &= n_0 X_0 + n_0 \delta X(t) + X_0 \delta n(t) + \delta n(t)\delta X(t) \end{aligned} \tag{47}$$

In the linearized model the first term on the RHS is neglected. The last term on the RHS can be neglected if:

$$\delta n(t)\delta X(t) \ll \min(n_0 \delta X(t), X_0 \delta n(t)). \tag{48}$$

When sufficiently large deviations are introduced, this condition will not be valid anymore. To study the limit of the linear approximation, we studied the dynamic response of the system without control drums, following a step reactivity insertion. An example is depicted in Fig. 9. Two reactivity steps, of 10 pcm and 100 pcm, were introduced to a critical reactor at 22 MWth.

As shown in the figure, each model reaches a different peak power. The nonlinear peak power is higher than the linear. The reason is that the nonlinear term $\delta\rho(t)\delta n(t)$ in the flux equation is a growth term (it has a positive sign). When this term is neglected, the growth rate of the flux is decreased, and accordingly also the peak power.

While the peak power difference for the 10 pcm is very small ($< 0.5\%$), for the 100 pcm case this difference ($\sim 6\%$) is probably not negligible. In both cases, after about 200 seconds the power converges to a new equilibrium (following a temperature change), and the two models agree. However, in terms of the operational and safety performance of the reactor, this type of under-prediction in the peak power of the transient is likely not acceptable.

The limitation of the linearized model depends on the steady-state power level, as demonstrated in Fig. 10. Here, the difference in the peak power is shown for various step reactivity insertion values:

$$\frac{\delta P_{max}}{P_0} = \frac{P_{max}^{nonlinear} - P_{max}^{linear}}{P_0} \tag{49}$$

It can be seen that as power increases, the differences between the models increase. At a power of 20MWth, a 150 pcm insertion yields a difference above 20%. Even for power levels as low as 1MW, the differences become significant for large enough reactivity insertions.

From this result we might conclude that any practical control algorithm would need to account for the nonlinear dynamics of the reactor to prevent severe undershoot or overshoot of the power. Consequently, some augmentation to the traditional control methodology may be warranted. However, as we will see in the next section, the MPC performs quite well in spite of this. Nevertheless, we recommend considering improving this aspect of the models in future work.

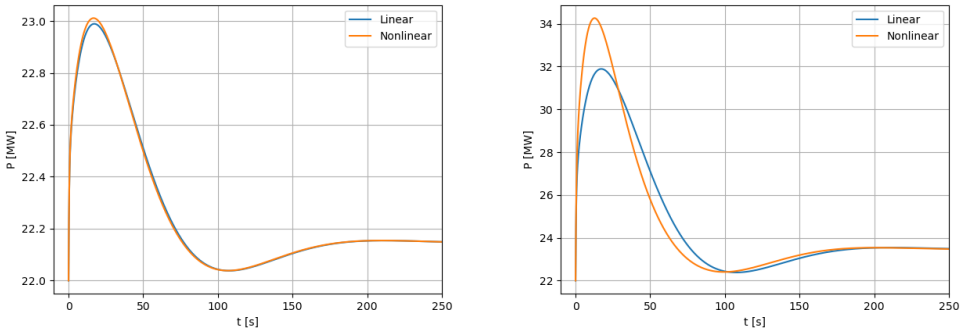

(a) 10 pcm **(b) 100 pcm**

Figure 9. Comparison of nonlinear and linearized models following a step reactivity insertion of 10 pcm (left) and 100 pcm (right).

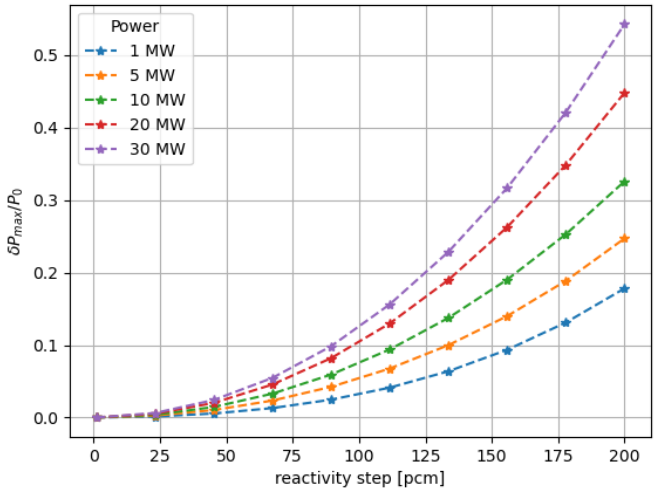

Figure 10. Peak power difference of nonlinear and linearized models, shown for increasing values of power and reactivity step insertions.

4. AUTONOMOUS CONTROL OF THE HOLOS REACTOR

4.1 Model Predictive Control

To solve the state-space control problem derived in Section 2 we use the MPC algorithm. MPC is an advanced method to control a process while satisfying a set of constraints [13]. It is based on an iterative finite-horizon optimization of the system (i.e. trajectory optimization). In the form presented here we focus on the linear, time-invariant state-space model derived in Section 2.3. To minimize an error between a desired set-point and predicted output, a control input is computed for a relatively short time horizon in the future by evaluating a cost function. This calculation is then repeated at each subsequent instant or time-window.

The basic theory of MPC is described here for completeness. The following derivation of MPC

is based largely on [14]. The state-space model derived in Eq. (19) is written as the following time-discretized linear system.

$$\mathbf{x_m}(k+1) = \mathbf{A_m}\mathbf{x_m}(k) + \mathbf{B_m}\mathbf{u}(k), \tag{50}$$

$$\mathbf{y}(k) = \mathbf{C_m}\mathbf{x_m}(k), \tag{51}$$

where k is the time step index, and $\mathbf{A_m}$, $\mathbf{B_m}$, and $\mathbf{C_m}$ are the discrete forms of $\mathbf{A_c}$, $\mathbf{B_c}$, and $\mathbf{C_c}$, respectively.

Applying a finite difference approximation to Eq. (51), yields

$$\mathbf{x_m}(k+1) - \mathbf{x_m}(k) = \mathbf{A_m}\left(\mathbf{x_m}(k) - \mathbf{x_m}(k-1)\right) + \mathbf{B_m}\left(\mathbf{u}(k) - \mathbf{u}(k-1)\right). \tag{52}$$

Next, we make use of the following simplifying notation

$$\Delta(\cdot)(k) = (\cdot)(k) - (\cdot)(k-1), \tag{53}$$

to yield

$$\Delta\mathbf{x_m}(k+1) = \mathbf{A_m}\Delta\mathbf{x_m}(k) + \mathbf{B_m}\Delta\mathbf{u}(k). \tag{54}$$

Note that the input to the state-space model is $\Delta\mathbf{u_m}(k)$. The next step is to connect $\Delta\mathbf{x_m}(k)$ to the output, $\mathbf{y_m}(k)$. To do so, a new state variable vector is defined as

$$\mathbf{x}(k) = \begin{bmatrix} \Delta\mathbf{x_m}(k)^T & \mathbf{y}(k) \end{bmatrix}^T. \tag{55}$$

Note that

$$\begin{aligned} \mathbf{y}(k+1) - \mathbf{y}(k) &= \mathbf{C_m}\left(\Delta\mathbf{x_m}(k+1)\right) \\ &= \mathbf{C_m}\mathbf{A_m}\Delta\mathbf{x_m}(k) + \mathbf{C_m}\mathbf{B_m}\Delta\mathbf{u}(k). \end{aligned} \tag{56}$$

Combining Eqs. (54) and (56) leads to the following discretized state-space model:

$$\overbrace{\begin{bmatrix} \Delta\mathbf{x_m}(k+1) \\ \mathbf{y}(k+1) \end{bmatrix}}^{\mathbf{x}(k+1)} = \overbrace{\begin{bmatrix} \mathbf{A_m} & \mathbf{o_m}^T \\ \mathbf{C_m}\mathbf{A_m} & 1 \end{bmatrix}}^{\mathbf{A}} \overbrace{\begin{bmatrix} \Delta\mathbf{x_m}(k) \\ \mathbf{y}(k) \end{bmatrix}}^{\mathbf{x}(k)} + \overbrace{\begin{bmatrix} \mathbf{B_m} \\ \mathbf{C_m}\mathbf{B_m} \end{bmatrix}}^{\mathbf{B}} \Delta\mathbf{u}(k), \tag{57}$$

$$\mathbf{y}(k) = \overbrace{\begin{bmatrix} \mathbf{o_m}^T & 1 \end{bmatrix}}^{\mathbf{C}} \begin{bmatrix} \Delta\mathbf{x_m}(k) \\ \mathbf{y}(k) \end{bmatrix}, \tag{58}$$

where $\mathbf{o_m} = \overbrace{\begin{bmatrix} 0 & 0 & \dots & 0 \end{bmatrix}}^{n_1}$ is the null vector; n_1 is the dimension of $\mathbf{x_m}$; and $\mathbf{A}$, $\mathbf{B}$, and $\mathbf{C}$ are called the augmented model, that will be used in the design of the predictive control.

Assuming that at the sampling instant k_i, where $k_i > 0$, the state variable vector $\mathbf{x}(k_i)$ is available through measurement, then the state $\mathbf{x}(k_i)$ provides the current plant information. The future control trajectory is denoted by

$$\Delta\mathbf{u}(k_i),\ \Delta\mathbf{u}(k_i+1),\ \dots,\ \Delta\mathbf{u}(k_i+N_c-1), \tag{59}$$

where N_c is called the *control horizon*–dictating the number of parameters used to capture the future *control trajectory*. With the information given in $\mathbf{x}(k_i)$, the future state variables are predicted for N_p number of samples, where N_p is called the prediction horizon. N_p is also the length of the optimization window. We denote the future state variables as

$$\mathbf{x}(k_i|k_i),\ \mathbf{x}(k_i+1|k_i),\ \ldots,\ \mathbf{x}(k_i+N_p|k_i), \tag{60}$$

where $\mathbf{x}(k_i+m|k_i)$ is the predicted state variable at k_i+m with given current plant information $\mathbf{x}(k_i)$. The control horizon N_c is chosen to be less than (or equal to) the prediction horizon N_p.

It is possible to denote the state-space model for the prediction horizons as follows:

$$\mathbf{Y} = \mathbf{F}\mathbf{x}(k_i) + \mathbf{\Phi}\Delta\mathbf{U}, \tag{61}$$

where

$$\mathbf{Y} = \begin{bmatrix} \mathbf{y}(k_i+1|k_i) & \cdots & \mathbf{y}(k_i+N_p|k_i) \end{bmatrix}^T, \tag{62}$$

$$\Delta\mathbf{U} = \begin{bmatrix} \Delta\mathbf{u}(k_i) & \cdots & \Delta\mathbf{u}(k_i+N_c-1) \end{bmatrix}^T, \tag{63}$$

$$\mathbf{F} = \begin{bmatrix} \mathbf{CA} \\ \vdots \\ \mathbf{CA}^{N_p} \end{bmatrix}, \tag{64}$$

$$\mathbf{\Phi} = \begin{bmatrix} \mathbf{CB} & 0 & 0 & \cdots & 0 \\ \mathbf{CAB} & \mathbf{CB} & 0 & \cdots & 0 \\ \mathbf{CA}^2\mathbf{B} & \mathbf{CAB} & \mathbf{CB} & \cdots & 0 \\ \vdots & & & & \\ \mathbf{CA}^{N_p-1}\mathbf{B} & \mathbf{CA}^{N_p-2}\mathbf{B} & \mathbf{CA}^{N_p-3}\mathbf{B} & \cdots & \mathbf{CA}^{N_p-N_c}\mathbf{B} \end{bmatrix}. \tag{65}$$

For a given set-point signal (or reference trajectory), the objective of the predictive control system is to bring the predicted output as close as possible to the set-point signal. It is assumed that the set-point signal remains constant in the optimization window. This objective is then translated into an input to find the "best" control parameter vector $\Delta\mathbf{U}$ such that an error function between the set-point and the predicted output is minimized. The cost function J, that reflects the control objective, is defined as follows:

$$J = (\mathbf{R_s} - \mathbf{Y})^T\,(\mathbf{R_s} - \mathbf{Y}) + \Delta\mathbf{U}^T\bar{\mathbf{R}}\Delta\mathbf{U}, \tag{66}$$

where the data vector $\mathbf{R_s}^T$ contains the set-point information $r(k_i)$ as follows:

$$\mathbf{R_s}^T = \bar{\mathbf{R}}_\mathbf{s} r(k_i) = \overbrace{\begin{bmatrix} 1 & 1 & \cdots & 1 \end{bmatrix}}^{N_p} r(k_i). \tag{67}$$

In Eq. (66), the first term is linked to the objective of minimizing the errors between the predicted output $\mathbf{Y}$ and the set-point signal $\mathbf{R_s}$. The second term reflects the consideration given to the size of $\Delta\mathbf{U}$ when the objective function J is made to be as small as possible. $\bar{\mathbf{R}}$ is a diagonal matrix in the form that $\bar{\mathbf{R}} = r_w\mathbf{I}_{N_c\times N_c}$ $(r_w \geq 0)$ where r_w is used as a tuning parameter for the desired

closed-loop performance. To find the optimal control input that will minimize J, J is expressed as follows by using Eqs. (61) and (66):

$$J = (\mathbf{R_s} - \mathbf{F}\mathbf{x}(k_i))^T (\mathbf{R_s} - \mathbf{F}\mathbf{x}(k_i)) - 2\Delta\mathbf{U}^T\mathbf{\Phi}^T (\mathbf{R_s} - \mathbf{F}\mathbf{x}(k_i)) + \Delta\mathbf{U}^T \left(\mathbf{\Phi}^T\mathbf{\Phi} + \bar{\mathbf{R}}\right)\Delta\mathbf{U}. \tag{68}$$

According to the extreme value theory of functions, when the derivative of J with respect to $\Delta\mathbf{U}$ (i.e. $\partial J/\partial\Delta\mathbf{U}$) is zero, the objective function J gets its extreme values. The first derivative of J is

$$\frac{\partial J}{\partial \Delta\mathbf{U}} = 2\mathbf{\Phi}^T (\mathbf{R_s} - \mathbf{F}\mathbf{x}(k_i)) + 2\left(\mathbf{\Phi}^T\mathbf{\Phi} + \bar{\mathbf{R}}\right)\Delta\mathbf{U}. \tag{69}$$

From relation of $\partial J/\partial\Delta\mathbf{U} = 0$, the optimal solution is found as follows:

$$\begin{aligned}\Delta\mathbf{U} &= \left(\mathbf{\Phi}^T\mathbf{\Phi} + \bar{\mathbf{R}}\right)^{-1}\mathbf{\Phi}^T (\mathbf{R_s} - \mathbf{F}\mathbf{x}(k_i)) \\ &= \left(\mathbf{\Phi}^T\mathbf{\Phi} + \bar{\mathbf{R}}\right)^{-1}\mathbf{\Phi}^T \left(\bar{\mathbf{R}}_\mathbf{s} r(k_i) - \mathbf{F}\mathbf{x}(k_i)\right),\end{aligned} \tag{70}$$

where the matrix $\left(\mathbf{\Phi}^T\mathbf{\Phi} + \bar{\mathbf{R}}\right)^{-1}$ is called the Hessian matrix in the optimization literature, and $\left(\mathbf{\Phi}^T\mathbf{\Phi} + \bar{\mathbf{R}}\right)^{-1}$ is assumed to exist.

Although the optimal parameter vector $\Delta\mathbf{U}$ contains the controls $\Delta\mathbf{u}(k_i)$, $\Delta\mathbf{u}(k_i + 1)$, ..., $\Delta\mathbf{u}(k_i + N_c - 1)$, with the receding horizon control principle, the first sample of this sequence, i.e. $\Delta\mathbf{u}(k_i)$, is implemented only while ignoring the rest of the sequence. When the next sample period arrives, the more recent measurement is taken to form the state vector $\mathbf{x}(k_i + 1)$ for calculation of the new sequence of control signal. This procedure is repeated in real time to give the receding horizon control law.

It should be noted that Eq. (70) is used for an unconstrained problem. However, in nearly all practical applications there are constraints imposed by the physical system that must be taken into account. There are several types of constraints frequently encountered in control applications. The first two types deal with constraints imposed on the control variables $\mathbf{u}(k)$ and $\mathbf{\Delta u}(k)$. The third type of constraint deals with the output, $\mathbf{y}(k)$, or the state variable, $\mathbf{x}(k)$.

4.1.1 MPC with constraints

In our application, three kinds of constraints are applied to the drum rotation $\mathbf{s}$, drum rotation rate $\mathbf{u}$, and drum rotation acceleration $\Delta\mathbf{u}/\Delta t$. It should be noted that these constraints are assumed because they have not been determined in the reactor design, yet. In reality, the constraints should be first based on the mechanical performance of the drum rotation system, and secondarily on technical specification limits for the operation that should satisfy safety and operational performance requirements. The numerical values of the constraints are listed in Table 4. An absorber material is placed on one side of the control drum as depicted in Fig. 3. The reactivity worth of the drum has the minimum and maximum worth when the drum faces outward and inward directions, respectively. Therefore, the drum rotation angle is constrained between 0 to 180°. This is equivalent to assuming symmetry about the fully inserted position. From [1], this is generally true, although this is not always the case. Future work will focus on using more complex control algorithms and reactivity worth curves for the drums. The rotation rate and angular acceleration are constrained within ±1°/s and ±1°/s^2, respectively.

Table 4. Applied constraints to Holos reactor control

Parameters	Constraints
Control drum rotation (deg)	$0 \leq \mathbf{s} \leq 180$
Control drum rotation rate (deg/s)	$-1.0 \leq \mathbf{u} \leq 1.0$
Control drum rotation acceleration (deg/s^2)	$-1.0 \leq \Delta\mathbf{u}/\Delta t \leq 1.0$

To incorporate the design constraints into the control problem, it is necessary to translate the constraints into linear inequalities. The constraints are taken into consideration for each moving horizon window. Since the MPC problem is formulated and solved in the framework of the receding horizon control, the constraints on the rate of change are expressed as

$$\Delta\mathbf{u}^{min} \leq \Delta\mathbf{u}(k_i) \leq \Delta\mathbf{u}^{max}, \tag{71}$$

where the superscripts *min* and *max* denote the minimum and the maximum constraints, respectively.

The constraints are defined within the control horizon so that it can be expressed in terms of function $\Delta\mathbf{U}$ as follows:

$$\Delta\mathbf{U}^{min} \leq \Delta\mathbf{U} \leq \Delta\mathbf{U}^{max}, \tag{72}$$

where $\Delta\mathbf{U}^{min}$ and $\Delta\mathbf{U}^{max}$ are column vectors with N_c elements of $\Delta\mathbf{u}^{min}$ and $\Delta\mathbf{u}^{max}$, respectively.

The constraints then need to be decomposed into two parts to reflect the lower and the upper limit. This is expressed as follows:

$$\begin{bmatrix} -\mathbf{I} \\ \mathbf{I} \end{bmatrix} \Delta\mathbf{U} \leq \begin{bmatrix} -\Delta\mathbf{U}^{min} \\ \Delta\mathbf{U}^{max} \end{bmatrix}, \tag{73}$$

where $\mathbf{I}$ is the identity matrix, and its size depends on N_c and $\mathbf{u}$.

This procedure also applies to the control input and output constraints. All constraints are expressed in terms of $\Delta\mathbf{U}$. In the case of the manipulated constraints (or control input), it is written as follows:

$$\begin{bmatrix} \mathbf{u}(k_i) \\ \mathbf{u}(k_i+1) \\ \vdots \\ \mathbf{u}(k_i+N_c+1) \end{bmatrix} = \begin{bmatrix} \mathbf{I} \\ \mathbf{I} \\ \vdots \\ \mathbf{I} \end{bmatrix} \mathbf{u}(k_i-1) + \begin{bmatrix} \mathbf{I} & 0 & \cdots & 0 \\ \mathbf{I} & \mathbf{I} & \cdots & 0 \\ \vdots & \vdots & \ddots & \vdots \\ \mathbf{I} & \mathbf{I} & \cdots & \mathbf{I} \end{bmatrix} \begin{bmatrix} \Delta\mathbf{u}(k_i) \\ \Delta\mathbf{u}(k_i+1) \\ \vdots \\ \Delta\mathbf{u}(k_i+N_c-1) \end{bmatrix}. \tag{74}$$

Equation (74) is rewritten in a compact matrix form with appropriate matrices $\mathbf{C}_1$ and $\mathbf{C}_2$ as follows:

$$\begin{aligned} -\left[\mathbf{C}_1\mathbf{u}(k_i-1) + \mathbf{C}_2\Delta\mathbf{U}\right] &\leq -\mathbf{U}^{min} \\ \left[\mathbf{C}_1\mathbf{u}(k_i-1) + \mathbf{C}_2\Delta\mathbf{U}\right] &\leq \mathbf{U}^{max}. \end{aligned} \tag{75}$$

Using Eq. (61), the output constraints are expressed in terms of $\Delta\mathbf{U}$ as:

$$\mathbf{Y}^{min} \leq \mathbf{F}\mathbf{x}(k_i) + \mathbf{\Phi}\Delta\mathbf{U} \leq \Delta\mathbf{Y}^{max}. \tag{76}$$

Finally, the MPC in the presence of constraints is proposed as finding $\Delta\mathbf{U}$ that minimizes the quadratic cost function

$$\begin{aligned} J = &\left(\mathbf{R_s} - \mathbf{F}\mathbf{x}(k_i)\right)^T \left(\mathbf{R_s} - \mathbf{F}\mathbf{x}(k_i)\right) \\ &- 2\Delta\mathbf{U}^T\mathbf{\Phi}^T \left(\mathbf{R_s} - \mathbf{F}\mathbf{x}(k_i)\right) + \Delta\mathbf{U}^T \left(\mathbf{\Phi}^T\mathbf{\Phi} + \bar{\mathbf{R}}\right)\Delta\mathbf{U}. \end{aligned} \tag{68 revisited}$$

Subject to the inequality constraints:

$$\begin{bmatrix} \mathbf{M}_1 \\ \mathbf{M}_2 \\ \mathbf{M}_3 \end{bmatrix} \Delta\mathbf{U} \leq \begin{bmatrix} \mathbf{N}_1 \\ \mathbf{N}_2 \\ \mathbf{N}_3 \end{bmatrix}, \tag{77}$$

where the matrices are

$$\mathbf{M}_1 = \begin{bmatrix} -\mathbf{C}_2 \\ \mathbf{C}_2 \end{bmatrix};\ \mathbf{M}_2 = \begin{bmatrix} -\mathbf{I} \\ \mathbf{I} \end{bmatrix};\ \mathbf{M}_3 = \begin{bmatrix} -\mathbf{\Phi} \\ \mathbf{\Phi} \end{bmatrix};$$

$$\mathbf{N}_1 = \begin{bmatrix} -\mathbf{U}^{min} + \mathbf{C}_1\mathbf{u}(k_i - 1) \\ \mathbf{U}^{max} - \mathbf{C}_1\mathbf{u}(k_i - 1) \end{bmatrix};\ \mathbf{N}_2 = \begin{bmatrix} -\Delta\mathbf{U}^{min} \\ \Delta\mathbf{U}^{max} \end{bmatrix};\ \mathbf{N}_3 = \begin{bmatrix} -\mathbf{Y}^{min} + \mathbf{F}\mathbf{x}(k_i) \\ \mathbf{Y}^{max} - \mathbf{F}\mathbf{x}(k_i) \end{bmatrix}.$$

This problem is a representative mathematical optimization problem, where Quadratic Programming (QP) [15] may be used to solve Eq. (68) with the inequalities in Eq. (77). Algorithm 1 summarizes the MPC algorithm described in this section.

Algorithm 1 MPC algorithm

1: Construct state-space model in Eq. (19).
2: Convert state-space model to time-discrete model.
3: Determine N_c, N_p, and $\bar{\mathbf{R}}$.
4: Calculate $\mathbf{F}$ and $\mathbf{\Phi}$ in Eqs. (64) and (65).
5: **for** time steps k_i **do**
6: Set prediction set-point vector $\mathbf{R_s}$.
7: **if** problem is constrained **then**
8: Calculate $\Delta\mathbf{U}$ by minimizing Eq. (68) subject to Eq. (77) through QP.
9: **else**
10: Calculate $\Delta\mathbf{U}$ in Eq. (70).
11: **end if**
12: Choose the first control input $\Delta\mathbf{u}(k_i)$ from $\Delta\mathbf{U}$.
13: Update state and output vectors $\mathbf{x}$ and $\mathbf{y}$ using Eqs. (57) and (58).
14: **end for**

4.2 Numerical Results

In this section, Single-Input and Multiple-Output (SIMO) and Multiple-Input and Multiple-Output (MIMO) problems are solved to test the MPC controller. The state-space model with the MPC algorithm is implemented in a test code.

4.2.1 Single-Input–Multiple-Output Example

The first scenario we consider is depicted, along with the control result, in Fig. 11a. In this contrived power maneuver we consider the SIMO case. The reference power trajectory is chosen to have a power ramp rate of $\pm 10\% P_r$/min. The power transition from 5 min to 15 min and from 40 min to 50 min. In this simulation, it is assumed that all control drums are rotated simultaneously.

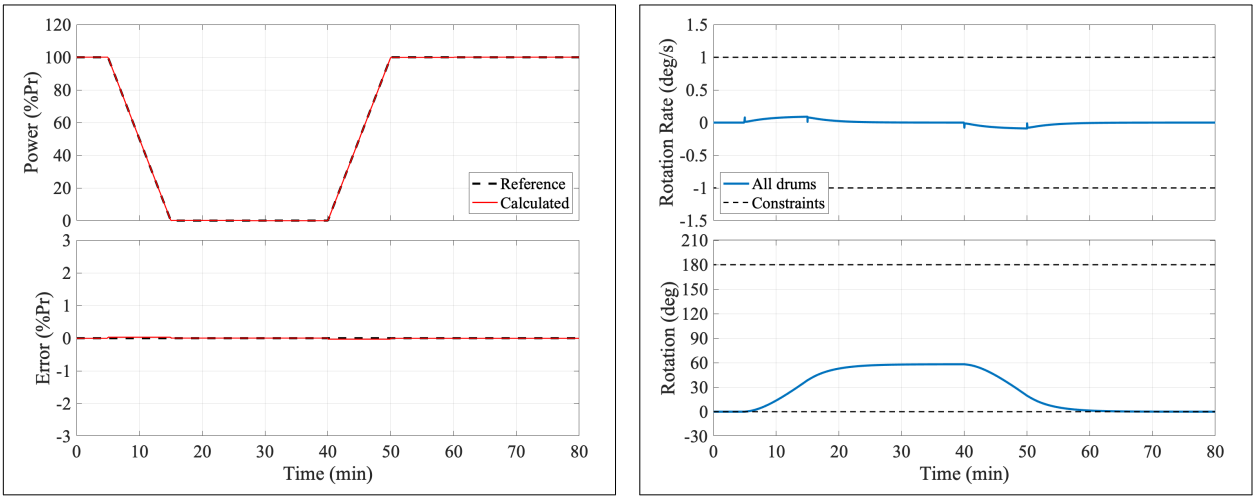

(a) Power and error **(b) Control inputs**

Figure 11. Power and control input for SIMO example

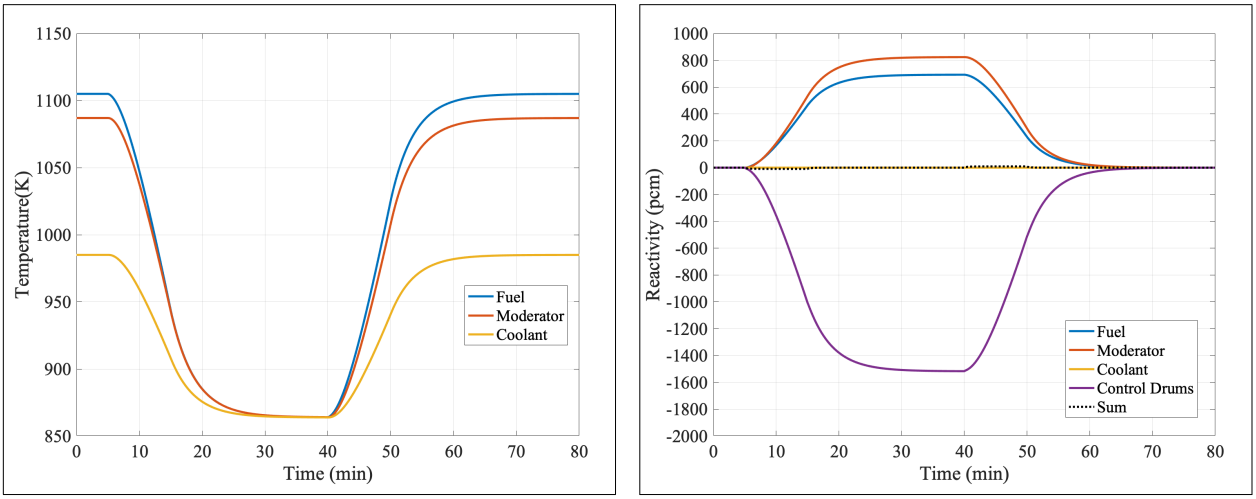

(a) Temperature **(b) Reactivity change**

Figure 12. Temperature and reactivity changes for SIMO example

As shown in Fig. 11a, the MPC controller follows the desired power accurately. There is no noticeable error between the reference power and calculated power. Fig. 11b shows the rotation and rotation rate of the control drum. The calculated control actions satisfy both of the given constraints for rotation and rotation rate.

Fig. 12 presents the evolution of the temperatures and reactivity components during the maneuver. The temperature overall lags the power trajectory–as predicted by the Bode diagram in Fig. 6.

There are three passive temperature reactivity feedback mechanisms through the fuel, moderator, and coolant. However, the reactivity coefficient for the coolant is assumed to be 0.0 in these calculations. The reactivity feedback from both the fuel and moderator are significant, and this is because the temperature reactivity coefficients of the fuel and moderator are comparable. This is shown in Table 2. The temperatures of both materials change significantly during the load follow maneuver. When the power is changed from $0\%P_r$ to $100\%P_r$, the temperature changes of the fuel and moderator are more than 200 K. The power level reaches $0\%P_r$ at 15 min, and about 1000 pcm of reactivity is required up to this time. However, there are several lasting reactivity perturbations from the fuel and moderator. The additional external reactivity must be controlled by using the control drum, or the other control mechanisms, to compensate for the positive reactivities between 15 min and 40 min. The maximum external reactivity required for this maneuver is -1517 pcm at 40 min. From this simulation, it is concluded that it is necessary to have ±1517 pcm of external reactivity to control the Holos reactor between $0\%P_r$ and $100\%P_r$. This means that the $10\%P_r$/min ramp rate requires a reactivity insertion rate that is at least ~151.7 pcm/min. The available total reactivity and the maximum reactivity insertion rate are summarized in Table 5. The maximum reactivity insertion rate is calculated based on rotation rate constraint, 1°/s. When all control drums are used in the reactivity control, there is more than enough margin to follow $\pm 10\%P_r$/min between 0 to $100\%P_r$.

Table 5. Reactivity insertion capability of control drums

# of control drums	Differential reactivity worth (pcm/deg)	Available total reactivity worth (pcm)	Maximum reactivity insertion rate (pcm/min)	Estimated power ramp rate ($\%P_r$/min)
1	-2.78	-500	±167	11.0
2	-7.33	-1319	±440	29.0
4	-16.11	-2900	±967	63.7
8	-26.11	-4700	±1567	103.3

4.2.2 Multiple-Input–Multiple-Output Example

In the SIMO example, it is assumed that all control drums are rotated with a single type of control input. In practice, this may not be the best way to control the Holos reactor. There is also the possibility to operate these control drums separately if so desired. If an operator wants to change a small amount of power or if it is necessary to respond to a very small external disturbance, it would be better to control reactivity using only one drum instead of rotating all drums simultaneously. By using a single drum it is possible to control the reactivity, and therefore, the power more precisely. In other cases, it may be preferred to reduce the number of irradiated control drums because it could become necessary to replace a drum if the absorber material is depleted significantly during operation, or it may be desired to shape the core power asymmetrically in some way for other reasons like continuing operation in a degraded state.

One of the strengths of MPC is that it can easily accommodate a constrained MIMO problem. For this case the MPC controller could give a solution, if it is necessary, to operate the control drums separately. In the second numerical example studied, the various power ramp rates are chosen from $1\%P_r$ up to $80\%P_r$. Fig. 13a shows the hypothetical power maneuver. The fastest ramp rate of the surveyed FPO requirements is $20\%P_r$ [1]. However, $40\%P_r$ and 80 $\%P_r$ ramp rates are also tested

to assess the feasibility of the control scheme to perform operations well beyond what is required.

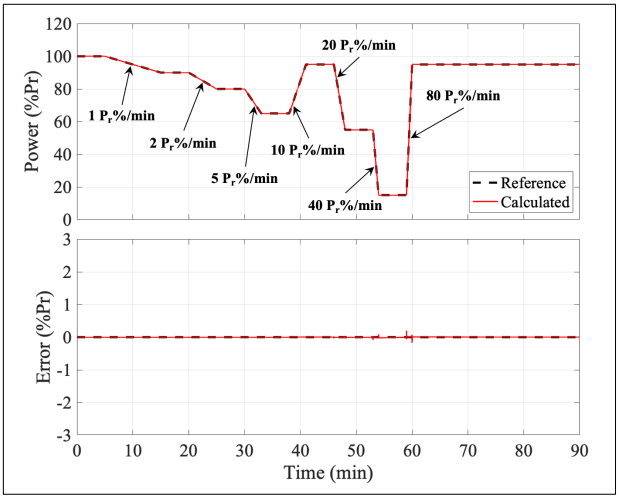

(a) Power and error

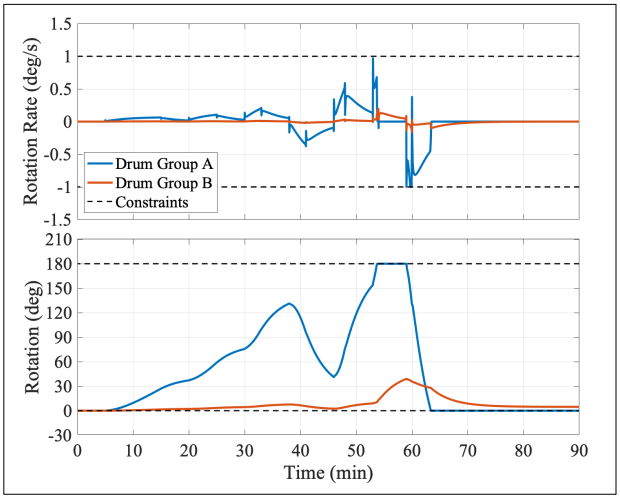

(b) Control inputs

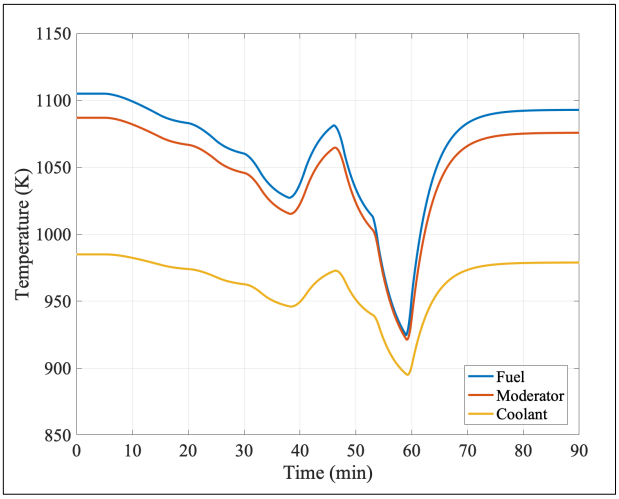

(c) Temperature

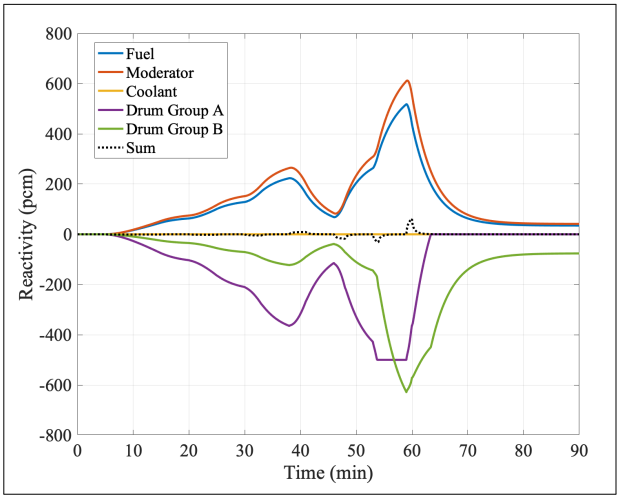

(d) Reactivity change

Figure 13. Control inputs and simulation outputs for MIMO example

In this MIMO simulation, two separate control inputs are assumed. One control drum is used for *Drum Group A* while four drums are used for *Drum Group B*. The MPC controller calculates separate inputs for *Group A* and *Group B*. When evaluating the cost function, the weight of *Group B* is specified to be 10 times more than *Group A*. This is so that the controller utilizes *Group A* more than *Group B*. It should be noted that it is necessary to study the reactivity more–particularly with high-fidelity models–when this kind of mixed number of control drums are used. The reason for this is the specific issue relating to a potential drum shadow effect where the sum of the reactivities from one drum and four drums are not identical to the reactivity worth when five drums are fully rotated because of this shadowing. Addressing this issue is a part of the future work and will require nonlinear and/or robust MPC implementations [16, 17, 18]. For now, we consider the coefficients given in Table 5 to be reasonable.

The simulation results for the MIMO example are shown in Fig. 13. Again, the calculated power

follows the desired reference power accurately. The error in power is less than $1\%P_r$ throughout the overall time domain. It is confirmed that even an $80\%P_r$/min ramp rate is achievable by using 5 drums. Fig. 13b shows the calculated control inputs for *Group A* and *Group B*. The results for the temperatures and reactivity components are presented in Figs. 13c and 13d. It is observed that *Group A* tends to move much more than *Group B*. Of course this was by design, since the weighting factor for *Group B* is larger than it is for *Group A*. We further observe that the MPC controller uses *Group A* extensively if the desired power and ramp rate are achievable by using just *Group A*. However, *Group B* is also used when *Group A* reaches a constraint such that no additional reactivity is available from *Group A*. This circumstance can be observed clearly between 53 min to 60 min.

This demonstrates that the MPC controller is capable of autonomous operation where the use of one drum bank is preferred over others. Therefore, we conclude that MPC is a feasible and flexible control algorithm for microreactor reactivity control capable of determining control solutions for SIMO as well as MIMO problems. This overall flexibility should be quite useful to enable optimal autonomous operations under a wide range of various core conditions.

4.2.3 Daily load following example

The simulated time of the two previous examples were 80 min and 90 min, respectively. This time interval is relatively short so that the ^{135}Xe dynamics may be neglected in these two simulations. As depicted in Fig. 4, the half-life of ^{135}I, which is the major parent nuclide of ^{135}Xe, is 6.7 hours. Because of ^{135}Xe's significant absorption cross section, the ^{135}Xe build-up effect would become important if the simulation time was longer, i.e. a day or a week.

If we are to consider longer periods of FPO, and modes of operation similar to peaking plants, then we expect the ^{135}Xe poisoning dynamics to be important physics to model in the controller. This shall be the case we consider next to determine the importance of modeling ^{135}Xe over longer time horizons, and to demonstrate that the MPC control strategy is feasible under these conditions as well.

The peaking power plant is a plant that generally runs only when there is a high demand for electricity. Our assumed scenario includes being shutdown for 8 hours overnight and then operating at full power for 16 hours during the day. We use a total simulated time of 5 days (or 120 hours). In the power transition between 0 to $100\%P_r$, a $20\%P_r$/min of ramp rate is used. The MPC controller is used for this simulation, and contains the MIMO model. Consequently, similar to the previous MIMO example, two control inputs are used. We again make use of the grouping where *Group A* controls one control drum, and *Group B* controls 4 drums. For the weights of the cost functions, we assume a value 4 times larger for *Group B* than for *Group A*.

First, we demonstrate the case of the controller where the model used to predict the system behavior is missing the ^{135}Xe dynamics to assess the effect of important missing physics in our model. In other words, the MPC controller solves the optimization problem through the state-space representation without ^{135}Xe while the control inputs from the MPC controller are applied to the "actual" reactor model which does have the ^{135}Xe physics. The power scenario of daily load following example and simulation results are shown in Fig. 14. As shown in Fig. 14a, there are considerable errors in the power from the MPC controller without ^{135}Xe. Immediately after the power transitions, the maximum error is reached, which is approximately $3\%P_r$. In this simulation, the MPC controller considers all the reactivity feedback is driven by the TH feedback. In fact, only a part of reactivity

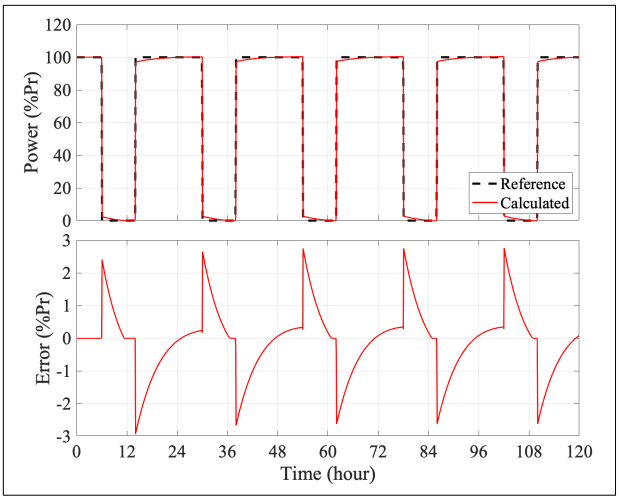

(a) Power and error

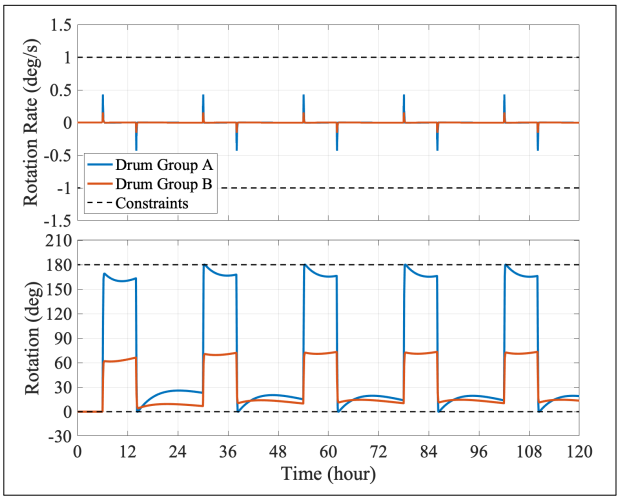

(b) Control inputs

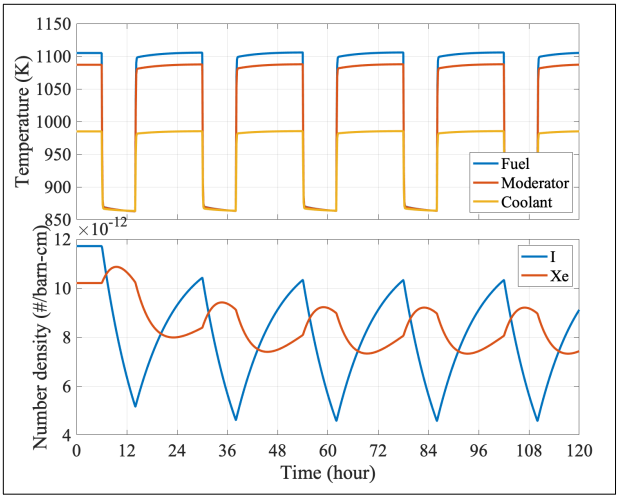

(c) Temperature and density

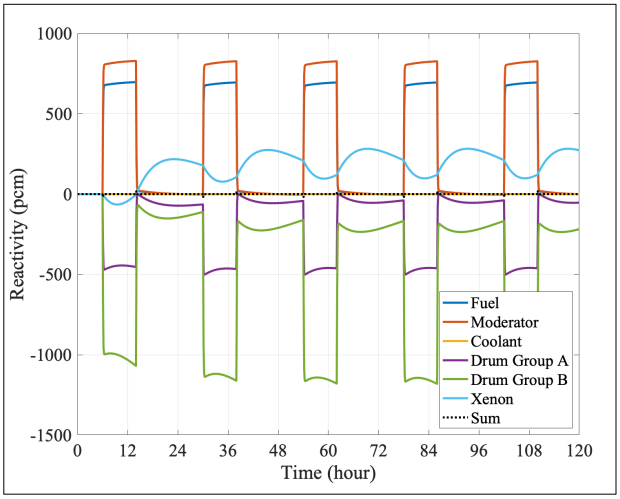

(d) Reactivity change

Figure 14. Simulation results for peaking power plant scenario with mismatch model

feedback is due to TH in this model, and the remainder is to ^{135}Xe. As a result, the MPC controller will *underestimate* the reactivity response of the reactor. This is illustrated in the results in Fig. 14d.

This underestimation of the reactivity results in the power errors observed in Fig. 14a. When the reactor is power is ramped down, the controller does not rotate the drums in as far as they need to be (compare Fig. 14b with Fig. 15b). The result is an overshoot of the power when ramping down. Conversely, When ramping up in power, the controller undershoots the power by not rotating the drums as far out as they need to be because the controller does not account for the additional negative reactivity of the ^{135}Xe.

The undershoot on power when ramping up results in the controller to continuously rotate the drums outward. Approximately 10 hours after reaching the full power, the power error gets flipped, and it reaches approximately $+0.3\%P_r$. This trend can be observed between 48 hours and 54 hours. In this period, the number density of ^{135}Xe is increasing from the decay of ^{135}I, so the drums should be rotated outward to decrease the imposed reactivity. The drums are rotated in the correct direction,

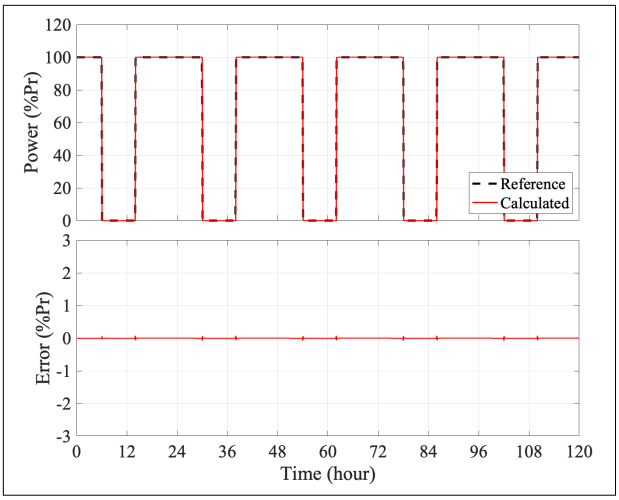

(a) Power and error

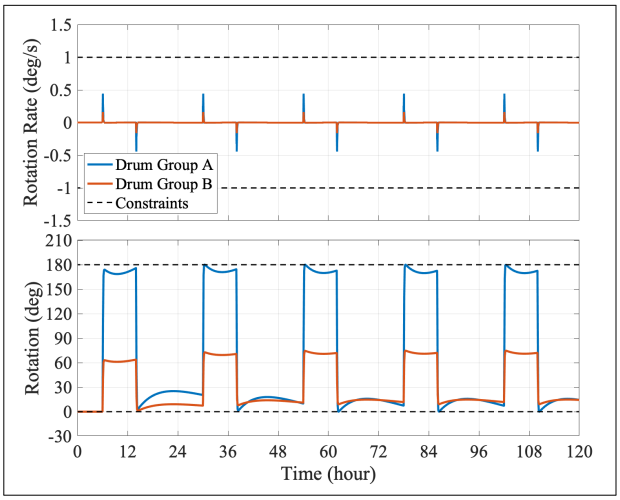

(b) Control inputs

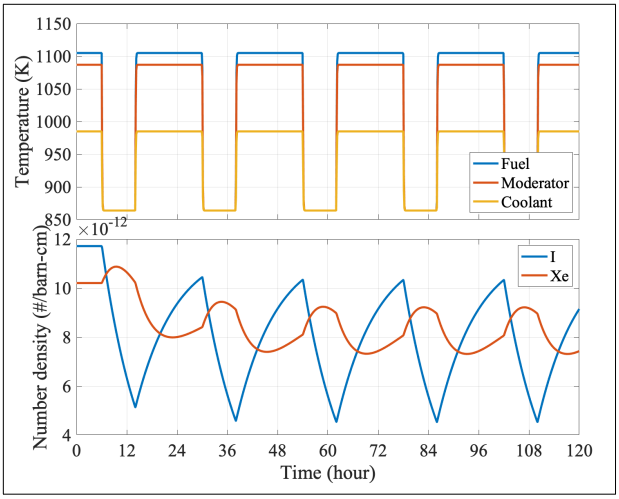

(c) Temperature and density

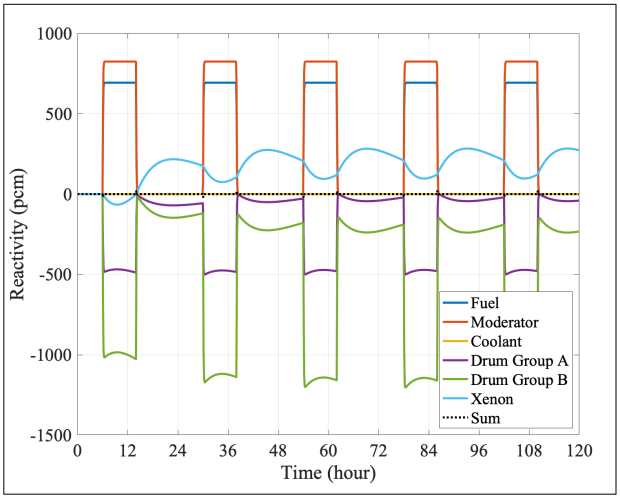

(d) Reactivity change

Figure 15. Simulation results for peaking power plant scenario

but the rotation rate is slower than it should be due to the absence of ^{135}Xe dynamics in the MPC controller. As a result, there is a slight overshoot of the power in this period. This demonstration shows qualitatively how the controller can be expected to behave when physics such as the ^{135}Xe dynamics, are missing in the state-space model.

The simulation results for the same scenario where the MPC controller does have the ^{135}Xe dynamics in the state-space model, are shown in Fig. 15. As may be observed in these results, the Holos reactor with the MPC controller successfully follows the desired power scenario with much less than $1\%P_r$ of power error. The results show that it is possible to follow the peaking power plant scenario by using 5 control drums. We wish to note here that this simulation is designed to show the capability to handle a MIMO problem using MPC. For actual operation, we recommended to control the power using all control drums to reduce local power peaking because ^{135}Xe can cause spatial oscillations if the control drum effects are localized. While we have not investigated this in detail yet, we expect that spatially radial ^{135}Xe oscillations are not likely to occur given the small

radial dimension of the core, and the relatively long mean free path of neutrons in graphite.

Fig. 15b shows that the drums should continuously rotate after reaching $0\%P_r$ or $100\%P_r$ to compensate for the reactivity from ^{135}Xe. Effectively, no steady-state condition is reached in this mode of operation. The temperatures and number densities for the daily load following operation are shown in Fig. 15c. Relative to the daily time-scale, the temperatures follow quickly to match the power, while the ^{135}I and ^{135}Xe lag considerably from the power transitions. Due to the delayed trends of ^{135}I and ^{135}Xe, it is important to have excess reactivity available in the control drums. The reactivity changes due to the TH feedback, ^{135}Xe, and control drums are shown in Fig. 15d. Here we observe that the reactivity change from ^{135}Xe is not as severe as the reactivity feedback from the fuel and moderator temperatures. Although, there is still a few hundred pcm of reactivity from ^{135}Xe–which is non-trivial. This reactivity can be compensated by continuously moving the drums even after the power goes equilibrium.

Generally, the ^{135}Xe build-up makes it difficult to restart operation since ^{135}Xe density increases after shutdown. If there is no way to give enough positive reactivity to the reactor, it is not possible to increase power until the amount of ^{135}Xe decreases to a certain point through decay. This phenomenon is well known, and is typically referred to as the ^{135}Xe dead time. The ^{135}Xe density typically reaches the maximum value after a few hours following shutdown. In the case of the Holos reactor, the elapsed time to reach peak ^{135}Xe is about 3.7 hours. For the commercial Pressurized Water Reactor (PWR) it is around 11 hours. This is due to the Holos reactor's small size, and considerably lower thermal power. Consequently, the ^{135}Xe does not have as significant of an effect on the reactor as it does in a PWR. The Holos reactor has a relatively small ^{135}Xe worth which is ~1000 pcm at the full power [2]. The peak ^{135}Xe density is about 10% higher than the ^{135}Xe density at the nominal full power condition. This amount of reactivity can be easily overcome with the current control drum design. The numerical results in Fig. 15 also support this argument. In other words, the Holos reactor does not have a significant ^{135}Xe dead-time so it would be capable of performing this type of load follow for most of its useful life. However, we have yet to quantify this exactly.

5. COMPARATIVE STUDY OF CONTROL ALGORITHMS

So far in this work we have focused on the use of the MPC controller. As we noted earlier, there are numerous control algorithms that may be used to control the Holos reactor drums. In this section, other control algorithms are briefly described. Following this description we provide some discussion and explanation as to why MPC is selected for Holos reactor control. We then present numerical results of the various controllers for the same power maneuvers to further support our preference for MPC.

5.1 Comparisons of Control Algorithms

5.1.1 Proportional-Integral-Derivative

PID is a control loop mechanism employing feedback that is widely used in industrial control systems and a variety of other applications requiring continuously modulated control [19]. A PID controller continuously calculates an error value and applies a correction based on proportional,

integral, and derivative terms (denoted P, I, and D respectively). PID is easy to implement and it does not require a complicated calculation. Because of the simplicity and generality, PID is used in many applications. However, it is only suitable for SISO problems. Moreover, the accuracy of PID is strongly dependent on the tuning of its parameters. Therefore, ensuring well tuned parameters over a broad range of system conditions is often the problem that must be addressed when adopting a PID controller.

5.1.2 Linear Quadratic Regulator

A Linear Quadratic Regulator (LQR) is also one of the well-known control methods that provides optimally controlled feedback gains for a closed-loop system [20]. This enables high performance of the system while maintaining its stability. In LQR, the system dynamics are described by a set of linear differential equations, and the cost is described by a quadratic function. The feedback control law is to minimize the quadratic cost-function. The multiple state variables and outputs can be readily considered in the system matrices and cost-function. Therefore, the LQR method is also capable of solving the MIMO problem. Another advantage is that the LQR algorithm reduces the amount of work done by the control systems engineer to optimize the controller. However, the tuned parameters of the controller are explicitly related to its accuracy and performance. Thus, if it is not well tuned, it will not perform well. This again makes this kind of controller less desirable for systems that might have a wide operational range that cannot be easily represented by the underlying model. Lastly, the adoption of nonlinear constraints, such as saturation, are generally not easily handled.

5.1.3 H_∞

H-infinity (H_∞) is another of the traditional control theories used in various industries [21]. An H_∞ controller finds necessary and sufficient conditions for the existence of a state feedback controller such that the closed-loop system corresponding to this controller is internally stable and satisfies a prescribed H_∞-norm constraint. Similar to the LQR, the H_∞ technique has the advantage in that it is applicable to a MIMO problem. The disadvantages of H_∞ techniques include the level of mathematical understanding needed to apply them successfully and the need for a reasonably good model of the system to be controlled. The resulting controller is also only optimal with respect to the prescribed cost function and does not necessarily represent the best controller. Like LQR, applying nonlinear constraints is generally not well-handled in this method.

Table 6. Summary of control algorithms

	PID	LQR	H_∞	MPC
Accuracy	Highly depends on tuning	Depends on tuning	Depends on tuning	Depends on tuning
Easy to tune?	Difficult	Easy	Easy	Easy
Able to handle constraints?	Not general	Not general	Not general	Yes
Able to handle MIMO?	Difficult	Yes	Yes	Yes
Calculation cost	Cheap	Expensive	Expensive	The most expensive

Table 6 summarizes the pros and cons of each algorithm including MPC. In the optimization

process, it is difficult to have a generally good solution for all cases because it is not clear how to determine what the optimum is in general. The optimum solution (or system input) would be the one that has the minimum error from the reference trajectory. However, the optimum solution would be different depending on the system state and its application. Therefore, it is usually necessary to use a tuning process in the control algorithms that considers an optimum over the full range of expected operational conditions.

In all of the controllers considered, tuning parameters are required. This means that it is possible to acquire similar levels of desired accuracy by using any controllers listed here, if tuning parameters are well defined. However, the accuracy of PID is quite sensitive so that it is necessary to put more effort to tune the PID controller's parameters. In LQR, H_∞, and MPC theories, cost functions are defined in their own way using a mathematical plant model. Then the algorithm finds the optimum solution to minimize their cost functions. Therefore, LQR, H_∞, and MPC controllers are not as highly sensitive to a plant model once the tuning parameter is well determined. Since PID does not have a similar process, the control input is totally dependent on the tuning parameter. The tuning parameter of PID should therefore be adjusted depending on the plant model. The PID can be also be tuned without having to use linearized model, which is perhaps its one advantage. However, nonlinear variants of the MPC controller do exist. Ultimately, this downside of PID makes it more difficult to tune the controller to get a desired performance. Thus, we argue, it would not be practical to use PID for Holos reactor control. In Section 5.2, this point is discussed more in the context of the simulation results.

In addition to tuning, MPC has a distinct strength in terms of accuracy compared to LQR and H_∞. MPC has a preview capability such that MPC can be more accurate in particular cases–provided the predictive model is accurate. As a result, MPC can easily incorporate future reference information into the control problem so that it is able to improve controller performance. Other controllers can also have a similar capability if a feed-forward algorithm is implemented into the system loop. However, some additional steps are necessary to implement this.

Another strength of MPC is that it can readily accommodate constraints on the control input or states. As described in Table 4, there are constraints due to physical limitations, and these control inputs or states should not exceed constraints. In this respect, MPC may be implemented with certain guarantees that would be applicable to safety requirements and representative of the actual physical asset. Essentially, in MPC the constraint is integrated into the evaluation of the cost function. In contrast, this is not the case for PID, LQR, and H_∞. For these controllers, it is necessary to adjust the tuning parameters so as not to exceed any constraints. Requiring the tuning parameters of these controllers to simultaneously ensure certain constraints are met, and optimal operation occurs, makes the overall tuning process quite a bit more challenging. Therefore, some degree of expertise is required–especially as the number of constraints grows. As an alternative way, if the control input is constrained in a system, then it is possible to force the control input to exist within the constraint when it should not be. When this occurs, it is called input saturation. It cannot be guaranteed that the system with the controller is stable and optimal when input saturation occurs [14, 22].

The controller for the Holos reactor should be capable of handling the MIMO problem. In doing so, greater flexibility of operation is possible. This enables both redundancy in the control system and the ability to consider more constraints. In Section 4.2, the MIMO problem is demonstrated

with the MPC controller. As mentioned previously, the LQR and H_∞ are also designed to solve the MIMO problem while considering the interactions between the inputs and outputs. Meaning, during the set up of the cost function and evaluation of the optimal solution, these controllers take into account all the interactions between system variables. A PID controller on the other hand, is not appropriate to use in a MIMO system because the multiple control loops would operate independently of each other. Therefore, again, the PID controller is not a good choice for our application.

Our last metric in the comparison of various controllers is the computational cost. In terms of the calculation cost, PID is the cheapest since it does not require to have a linear system and cost function minimization process. The PID controller only needs to know the errors of the output compared to the reference, and to be able to compute derivatives and integrals from this signal. LQR, H_∞, and MPC all must solve an optimization problem with a linear system and model-based cost function. Therefore, these three controllers are more complicated and computationally expensive than the PID controller. Moreover, MPC solves the finite time horizon optimization problem repeatedly for every time step in the time horizon. Meanwhile LQR and H_∞ only solve the optimization problem once for the whole time horizon (or infinite horizon). Therefore, MPC is the most expensive. The run times for the numerical results of the various controllers compared in the next section (Section 5.2 are summarized in Table 7, and support these conclusions.

In summary, MPC has many benefits against the other conventional control methods. MPC is accurate if the tuning parameters are well determined. Tuning the controller is not difficult, and the parameter is not highly sensitive to the plant model. Therefore, it is easy to get a desired accuracy using an MPC controller. MPC can also handle constrained MIMO problems easily. Because of these many advantages, we choose MPC for Holos reactor control. Of course, there is the downside of MPC that it requires a relatively larger amount of computer resources. In practice, the elapsed time for solving one scenario in this report is a few seconds on a single-core with an unoptimized implementation. Therefore, we may justify the relatively higher computational resource requirements because the calculation of the maneuvers for several hours of operation is still accomplished in seconds.

5.2 Numerical Results

In this section, the sensitivity of the controllers to the plant model is evaluated. The power scenario described in the MIMO example (Section 4.2) is used in this test. As discussed in Section 5, only MPC can handle a constrained problem. For a consistent comparison, the constraint is not used for all controllers because the constraint usually degrades the overall accuracy. PID, LQR, H_∞, and MPC are tuned based on the system using all control drums for power maneuvering. This case corresponds to Fig. 16a. All controllers show great accuracy with less than $1\%P_r$ deviation from the desired power. Therefore, it is confirmed that all the controllers tested in this work can have sufficient accuracy when the controller is tuned properly.

To test the controllers ability to handle differences in the plant model, the number of control drums is changed to four, two, and one. Recall that all the controllers are tuned to 8 drums. As shown in Figs. 16b to 16d, the PID controller shows significant oscillation in power output. This means that the PID tuning parameters should be changed depending on the reactor model as we conjectured. In practice, the reactor model may change or evolve for many different reasons (e.g. change in the

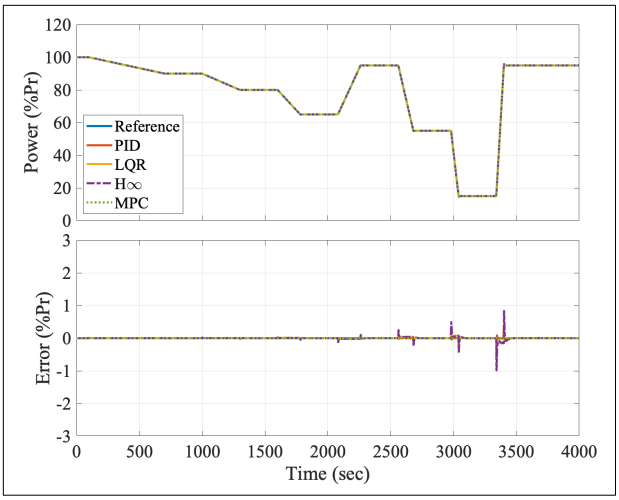

(a) Control using eight drums

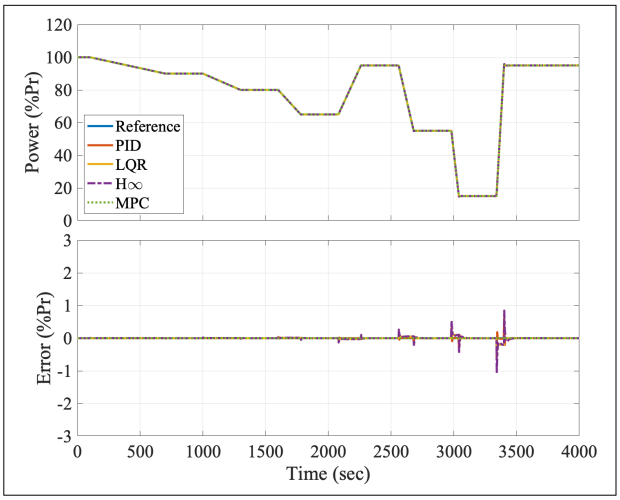

(b) Control using four drums

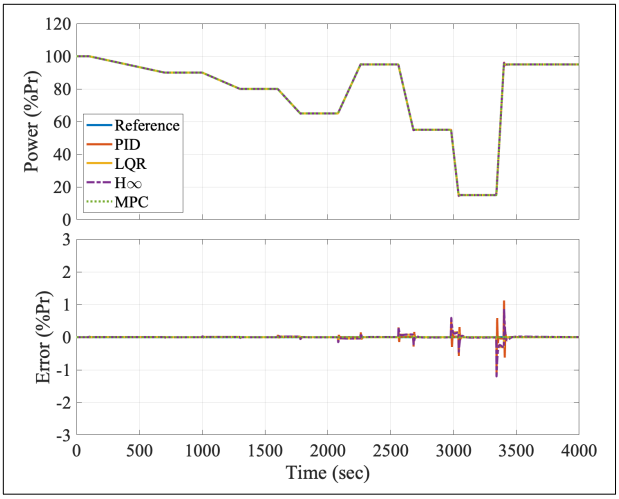

(c) Control using two drums

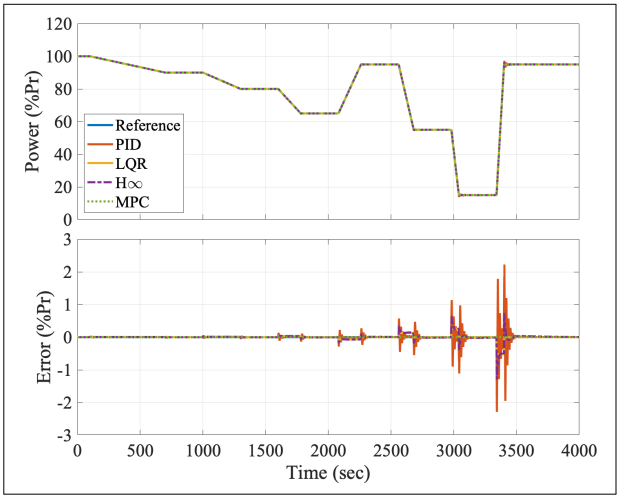

(d) Control using one drum

Figure 16. Comparison results for using different control algorithms

number of drums used for control, change in the initial power, changes in kinetics parameters, and TH parameters due to reactor condition change). Therefore, the controller should accommodate a varying reactor model, and use of a PID controller does not guarantee an accurate result. In contrast, LQR, H_∞, and MPC show consistently accurate results for all four tests. Therefore, the LQR and H_∞ controllers may be considered feasible, however, also recall that constraints were not used in these simulations and that a comparison of LQR, H_∞, and MPC controllers *with constraints* is warranted for a more thorough assessment.

Table 7 shows the elapsed time to simulate 4000 seconds of operation with 10ms time steps. As discussed in Section 5, PID shows the fastest results while MPC shows the slowest result. However, the elapsed time is just a few seconds. The amount of calculation time is readily acceptable with today's computing resources, and therefore MPC meets the real-time requirement for a controller.

Table 7. Comparison of elapsed time

Control Algorithm	Elapsed time (sec)
PID	0.09
LQR	0.16
H_∞	0.17
MPC	1.67

6. CONCLUSIONS AND FUTURE WORK

6.1 Conclusions

In this report, the state-space representation of the point kinetics and three-temperature TH model was developed for use with an MPC controller to autonomously control the Holos reactor for FPO. The control drums were used in the models to impose reactivity so that the model with the MPC controller was able to follow the prescribed power scenarios. To demonstrate FPO, various ranges of ramp rates and power envelopes were tested. It turns out that the reactor with the MPC controller successfully followed the desired power scenario. It is also confirmed that the reactor can be operated with the fastest ramp rate required (i.e. $20\%P_r$/min), and that the controller can perform power maneuvers well beyond these rates.

We also demonstrated the peaking power plant scenario, which required the incorporation of the ^{135}Xe dynamics into the state-space representation. Under these operational conditions, it was also confirmed that the Holos reactor could operate in this manner. This test demonstrates the feasibility of the Holos reactor to be utilized in multiple modes of FPO. It further demonstrated the ability of the controller to still provide control of the reactor even with important missing physics in the MPC model. In this case, the controller behaves conservatively, undershooting the desired power when ramping up, and overshooting the power when ramping down. The magnitude of the under/over-shoot of the power was approximately $3\%P_r$, which we consider to be significant. With the "correct" model (the model with ^{135}Xe), the MPC controller meets the desired power well within 1% error.

Finally, we presented a comparison of several control algorithms that have been applied previously in nuclear reactor problems. In this comparison, we summarized the basic strengths and weaknesses of each type of controller. Then results from numerical calculations for different scenarios to highlight the relative sensitivity of each type of controller to differences in the representation of the reactor system and the model were presented and discussed. In this comparison, we show that MPC is the most computationally expensive control method, and that all methods can prescribe accurate control solutions for FPO provided they are sufficiently tuned. The comparison also revealed that PID performs considerably more poorly than the other controllers when the system deviates from that used to tune the controller. From this comparison, overall we recommend the MPC controller as its computational cost is still well below the real-time calculation requirement, and offers several advantages such as the inclusion of constraints, nonlinear and time-varying representations, and robustness (i.e. the control performs well in the presence of noise) that we have not yet explored in detail.

In addition to these numerical demonstrations, we also studied the stability properties of the reactor

through the formalisms of the Bode diagram and root locus method. Both analytical techniques follow from the same state-space representation that can be used in the MPC controller. Thus, there inherent the same assumptions and limitations. In the Bode diagram, the reactor was observed to be insensitive to high-frequency reactivity oscillations and to respond in a manner similar to the zero-power reactor. The Bode diagram also revealed that the Holos reactor is less sensitive to low frequency reactivity oscillations (i.e. the presence of feedback reduces the gain). The feedback was also shown to shift the reactivity phase from positive to negative. The root locus method of evaluating the linear stability of the system showed no poles having a positive real component meaning that the physical system is linearly stable. Lastly, we compared time domain simulations of the linearized state-space model and the nonlinear model. This revealed a non-trivial differences in the predicted peak power following step reactivity insertions when the reactivity insertion was sufficiently large–in this case sufficiently large means as little as ~60pcm depending on the initial power level.

6.2 Future Work

From the work documented in this report, several opportunities for future studies were identified that will complement what was learned. Some of the shorter term activities that are recommended to enhance the present results are:

- Due to time constraints we were not able to perform the analytic evaluation of the state-space model in Sections 3.1 and 3.2 with the ^{135}Xe dynamics. For consistency and completeness, we wish to study this to ensure it does not significantly affect the present results.
- Another important metric in evaluating a controller is the stability margin. Therefore, calculation of the stability margin from the Bode diagram for the block diagram in Fig. 5 with and without the controller is desired to further assess the system's stability with the controller.
- The control variable assumed here was the drum rotation velocity, however, other choices exist such as the control drum position. Therefore, we propose comparing control of drum the velocity versus the drum position as a future activity.

In addition to these activities, there are several logical extensions of the work here that were not previously considered in the project planning:

- From the comparison between the linear and nonlinear models in Section 3.3, we confirmed that the nonlinearity of the plant model is important when a large perturbation is introduced to the reactor. From this work, it is recommended to use adaptive MPC or nonlinear MPC to minimize the error from linearization–or at the very least better quantify it.
- It was also demonstrated that MPC can handle a MIMO problem and can position drums differently from one another. This capability would be useful, but it is recommended to develop analytic models for control drum worth with any combination of drums for better accuracy. To deal with the analytic models, it is recommended that *adaptive* MPC be explored as it is well suited for this purpose.
- The core represents only one part of the microreactor system. Therefore, we wish to extend the system dynamics model studied here to include components from the power conversion

system.

- The microreactor will have additional constraints during operation for thermal and mechanical limits of the materials and other components, and, in particular, the turbine. Therefore, the ability of the MPC controller to accommodate these additional constraints should be assessed.
- In the analysis performed here we have presumed we have a high-quality signal for the power without noting the details of how this signal would be provided. In reality this signal will contain some noise. Therefore, we propose to also extend the MPC controller to incorporate Kalman filters as the traditional mechanism for enabling *robust MPC* [18].

Beyond the short term activities to solidify the work presented here, and the new activities to build on this work, there are the programmatic tasks already identified within the project. These activities include:

- the evaluation of higher fidelity transient simulations using the controller developed here;
- comparison of model fidelity on the accuracy of the controller;
- comparison of the MPC controller to the passive reactivity control mechanism.

There also exists some possible synergy across projects in the microreactor program. The capabilities developed here could be used to provide an extended capability of the TRANSFORM library [23] to model system dynamics with controllers. Another possible synergy would be to supply this control framework for use in the Microreactor AGile Non-nuclear Experimental Testbed (MAGNET) facility [24] to provide control of the heaters during experiments. The coefficients used here could be easily modified to enable MAGNET to explore the dynamics of several HTGR designs and collect experimental data that is more representative of a particular reactor design.

REFERENCES

[1] B. Kochunas, K. Barr, S. Kinast, and S. Choi. "Global and Local Reactivity Assessments for Passive Control Systems of Multi-module HTGR Special Purpose Reactors." Technical Report NURAM-2020-005-00, University of Michigan, Ann Arbor (2020).

[2] Stauff, N. and Lee, C. and Shriwise, P. and Miao, Y. and Hu, R. and Vegendla, P. and Fei, T. "Neutronic Design and Analysis of the Holos-Quad Concept." Technical report, Argone National Laboratory (2019).

[3] "ARPA-E | Transportable Modular Reactor." URL https://arpa-e.energy.gov/?q=slick-sheet-project/transportable-modular-reactor.

[4] N. E. Stauff, C. Lee, L. Zou, and C. Filippone. "Core Design of the Holos-Quad Micro Reactor." *Transactions of the American Nuclear Society*, **volume 123**, pp. 1067–1069 (2020). URL https://dx.doi.org/10.13182/T123-33105.

[5] A. Moisseytsev, J. J. Sienicki, L. Zou, and C. Filippone. "Helium Brayton Cycle Design and Analysis for the Holos-Quad Micro Reactor." *Transactions of the American Nuclear Society*, **volume 123**, pp. 1063–1066 (2020). URL https://dx.doi.org/10.13182/T123-33074.

[6] A. Lohkov. "Technical and Economic Aspects of Load Following with Nuclear Power Plants." Technical report, NEA/OECD, Vienna, Austria (2011).

[7] "Non-baseload Operation in Nuclear Power Plants: Load Following and Frequency Control Modes of Flexible Operation." Technical report, International Atomic Energy Agency, Vienna, Austria (2018). URL http://www.iaea.org/Publications/index.html.

[8] H. Brey. "Current status and future development of modular high temperature gas cooled reactor technology." Technical Report IAEA-TECDOC-1198, International Atomic Energy Agency, Vienna (2001).

[9] S. Choi, S. Kinast, V. Seker, C. Filippone, and B. Kochunas. "Preliminary Study of Model Predictive Control for Load Follow Operation of Holos Reactor." *Transactions of the American Nuclear Society*, **volume 122**, pp. 660–663 (2020). URL https://dx.doi.org/10.13182/T122-32327.

[10] N. Kastin, E. Meron, A. Kolin, and S. Kinast. "Nonlinear stability and limit cycles in xenon-induced reactor oscillations." *Progress in Nuclear Energy*, **volume 116**, pp. 168–179 (2019).

[11] D. Sivan, S. Kinast, S. Choi, V. Seker, E. Gilad, C. Filippone, and B. Kochunas. "Linear Stability Analysis of HTR-like Micro-reactors." *Trans Am Nucl Soc*, **volume 122** (2020).

[12] E. Cervi, A. Cammi, and A. Di Ronco. "Stability analysis of the Generation-IV nuclear reactors by means of the root locus criterion." *Progress in Nuclear Energy*, **volume 106**, pp. 316–334 (2018).

[13] C. E. García, D. M. Prett, and M. Morari. "Model predictive control: Theory and practice—A survey." *Automatica*, **volume 25**(3), pp. 335 – 348 (1989). URL http://www.sciencedirect.com/science/article/pii/0005109889900022.

[14] L. Wang. *Model predictive control system design and implementation using MATLAB®*.

Springer Science & Business Media, London, UK (2009).

[15] "Quadratic programming." URL https://en.wikipedia.org/wiki/Quadratic_programming.

[16] V. Adetola, D. DeHaan, and M. Guay. "Adaptive model predictive control for constrained nonlinear systems." *Systems & Control Letters*, **volume 58**(5), pp. 320–326 (2009).

[17] R. Findeisen and F. Allgöwer. "An introduction to nonlinear model predictive control." In *21st Benelux meeting on systems and control*, volume 11, pp. 119–141. The Netherlands: Technische Universiteit Eindhoven Veldhoven (2002).

[18] P. J. Campo and M. Morari. "Robust model predictive control." In *1987 American control conference*, pp. 1021–1026. IEEE (1987).

[19] "PID controller." URL https://en.wikipedia.org/wiki/PID_controller.

[20] "Linear–quadratic regulator." URL https://en.wikipedia.org/wiki/Linear\T1\textendashquadratic_regulator.

[21] "H-infinity methods in control theory." URL https://en.wikipedia.org/wiki/H-infinity_methods_in_control_theory.

[22] P. Hippe. *Windup in Control: Its Effects and Their Prevention*. Springer-Verlag, New York (2006).

[23] M. S. Greenwood. "TRANSFORM - TRANsient Simulation Framework of Reconfigurable Models." Computer Software (2017). URL https://github.com/ORNL-Modelica/TRANSFORM-Library.

[24] D. P. Guillen, H. Trellue, J. O'Brien, P. Sabharwall, R. S. Reid, T. Unruh, T. Jay Harrison, and T. L. Sham. "Development of a non-nuclear microreactor test bed." In *Transactions of the American Nuclear Society*, volume 121, pp. 1623–1626. American Nuclear Society, Washington D.C. (2019).